Mass and momentum transport in the Tilted Rocket Rig experiment

K. Ferguson,* K. M. Wang, and B. E. Morgan
Lawrence Livermore National Laboratory, 7000 East Avenue, Livermore, California 94550, USA

(Received 4 April 2023; accepted 7 September 2023; published 27 September 2023)

High-fidelity large eddy simulations of the inclined Rayleigh-Taylor instability in the Tilted Rocket Rig experimental configuration [Smeeton and Youngs, AWE Report No. O 35/87 (1987)] are performed using a tenth-order compact finite difference code. These simulations are analyzed for spatial distributions of turbulent kinetic energy, turbulent mass flux velocity, species mass fraction flux, species mass fraction variance, and Favre-averaged Reynolds stresses at two time instances, $t = 37$ ms and $t = 52$ ms. Additionally, the vertical distribution of the components of the unclosed budget equations over the center of the domain for these quantities are examined. The dominant terms of these budget equations are further decomposed to examine the principal contributions to these terms in each axis. Notably, the principal contribution to the horizontal turbulent mass flux velocity budget is found to be from a term which is commonly neglected in many Reynolds-averaged Navier-Stokes models.

DOI: 10.1103/PhysRevFluids.8.094502

I. INTRODUCTION

The Tilted Rocket Rig is a series of experiments conducted by Smeeton and Youngs [1] and Youngs [2] in the late 1980s. This experiment consisted of a tank which was filled with two fluids of differing density, with the less dense of the two fluids located above the more dense fluid. The tank was inclined at an angle relative to horizontal. The apparatus was then accelerated by rockets attached to the top of the tank. The acceleration vector from the rockets was inclined relative to the density gradient at the interface between the two fluids. This gives rise to the Rayleigh-Taylor [3–6] instability (RTI) at the interface between the two fluids. The RTI is a buoyancy-driven instability which leads to the growth of small perturbations on the interface. These perturbations grow into spikes of heavy fluid penetrating into the light fluid, and bubbles of light fluid penetrating into the heavy fluid. Eventually these bubbles and spikes begin to interact and form a region of mixed fluid. At the same time, in the Tilted Rocket Rig, a bulk overturning motion of the two fluids also occurs. This results in a plume of heavy fluid rising into the light fluid on one edge of the tank, and a plume of light fluid falling into the heavy fluid on the other.

While multiple fluid pairs and configurations were considered as part of the Tilted Rocket Rig experiments, the present work will focus on case 110. This case utilized potassium iodide (NaI) and hexane (C_6H_{14}) as the heavy and light fluids, respectively. Figure 1 depicts a time sequence of experimental photographs from the case 110 experiment (reproduced from Andrews *et al.* [7]). Examination of these photographs reveals that there are two main areas in which fluid mixing may take place in this configuration. The first may be observed at the far left and right of the experimental images. These are plumes of heavy fluid rising into the light fluid (left), and light fluid falling into the heavy fluid (right). Additionally, a region of mixing may be observed at the tilted interface in the center of the tank. This region undergoes mixing due to Rayleigh-Taylor instability, but also

*ferguson43@llnl.gov

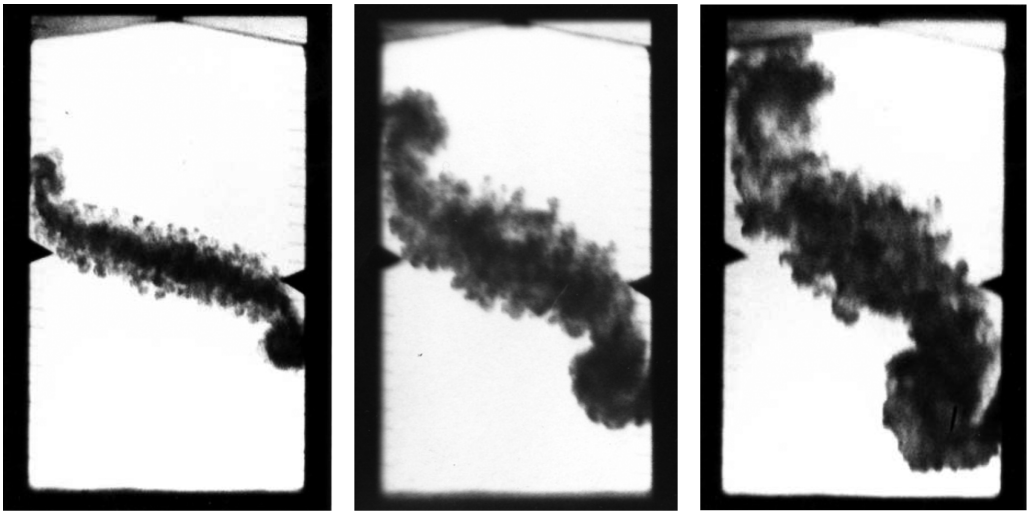

(a) (b) (c)

FIG. 1. Time sequence of experimental images from case 110 of Smeeton and Youngs [1]. Images reproduced from Andrews *et al.* [7]. British Crown Owned Copyright/AWE. Times are (a) $t = 45.3$ ms, (b) $t = 59.8$ ms, and (c) $t = 71.1$ ms.

experiences shear due to the relative motion of the upper (moving rightwards and downwards) and lower (moving leftwards and upwards) fluids as they undergo an overturning motion, as well as a stretching due to the rising and falling plumes of fluid.

This tilted rocket rig configuration is particularly interesting in the context of Reynolds-averaged Navier-Stokes (RANS) modeling endeavors. This configuration, in contrast to the more typical planar configurations, provides two-dimensional complexity with mixing and available experimental data for comparison and validation. This two-dimensionality provides a unique challenge for RANS models to accurately model turbulent transport in the presence of combined instability. Denissen *et al.* [8] proposed that this problem configuration was a useful one for the validation of Reynolds-averaged Navier-Stokes (RANS) models. Since then, Kokkinakis *et al.* [9], Xiao *et al.* [10], Xie *et al.* [11], and Xiao *et al.* [12] have utilized this configuration as a benchmark case for validating RANS models. The Tilted Rocket Rig configuration has also been studied using using implicit large eddy simulation (ILES) and direct numerical simulation (DNS) by Andrews *et al.* [7]. Denissen *et al.* [8] also presents ILES results as part of that work. These previous simulations have focused on integrated metrics, as well as a few turbulence quantities of relevance to BHR models. The present work expands upon this previous work by providing detailed statistics on a variety of turbulent variables with the goal of examining the dominant sources which govern the transport of mass and momentum in this configuration.

The present work seeks to examine the physics of the tilted rocket rig configuration in detail using high-fidelity artificial fluid large eddy simulations (AFLESs). This work will be presented in the following sections. First, the details of the numerical method used for this simulation is outlined in Sec. II. The configuration of the problem domain is presented in Sec. III. The first set of results, focused mainly on validation of the computational approach through mesh convergence studies and comparison with experiment, is shown in Sec. IV. Then detailed analysis of turbulent transport quantities and their budget equations is presented in Sec. V. Finally, a summary and conclusions are presented in Sec. VI.

II. NUMERICAL METHODS

The code used for these simulation is Miranda [13–16]. Miranda solves the compressible Navier-Stokes equations for a nonreacting, multicomponent mixture,

$$\frac{\partial \rho}{\partial t} + \frac{\partial (\rho u_i)}{\partial x_i} = 0, \tag{1}$$

$$\frac{\partial (\rho Y_\alpha)}{\partial t} + \frac{\partial (\rho Y_\alpha u_i)}{\partial x_i} = -\frac{\partial J_{\alpha,i}}{\partial x_i}, \tag{2}$$

$$\frac{\partial (\rho u_j)}{\partial t} + \frac{\partial (\rho u_i u_j)}{\partial x_i} = -\frac{\partial p}{\partial x_j} + \frac{\partial \sigma_{ij}}{\partial x_i} + \rho g_j, \tag{3}$$

$$\frac{\partial E}{\partial t} + \frac{\partial [(E+p)u_i]}{\partial x_i} = \frac{\partial (\sigma_{ij})}{\partial x_j} - \frac{\partial q_i}{\partial x_i} + \rho g_i u_i, \tag{4}$$

where ρ is the density, t is the time, u_i is the velocity along axis i, x_i is the spatial coordinate in axis i, Y_α is the mass fraction of species α, $J_{\alpha,i}$ is the diffusive mass flux of species α, p is the pressure, σ_{ij} is the viscous stress tensor, g_j is the gravitational body force in axis j, E is the total energy, and q_i is the heat flux in axis i. The diffusive mass flux is given by

$$J_{\alpha,i} = -\rho \left(D_\alpha \frac{\partial Y_\alpha}{\partial x_i} - Y_\alpha \sum_{k=1}^{N} D_k \frac{\partial Y_k}{\partial x_i} \right) \tag{5}$$

for $k = 1, 2, \ldots, N$ total species. The viscous stress tensor is

$$\sigma_{ij} = 2\mu S_{ij} + \left(\beta - \frac{2}{3}\mu \right) \frac{\partial u_i}{\partial x_i} \delta_{ij}, \tag{6}$$

where μ is the shear viscosity, β is the bulk viscosity, and δ_{ij} is the Kronecker delta. S_{ij} is the strain rate tensor, expressed as

$$S_{ij} = \frac{1}{2} \left(\frac{\partial u_i}{\partial x_j} + \frac{\partial u_j}{\partial x_i} \right). \tag{7}$$

The heat flux vector, q_i, is given as

$$q_i = -\kappa \frac{\partial T}{\partial x_i} + \sum_{k=1}^{N} h_k J_{k,i}, \tag{8}$$

where κ is the thermal conductivity and h_k is the enthalpy of species k where k is in the range $1, 2, \ldots, N$ for N fluids. The pressure, temperature, and enthalpy of each fluid component are obtained using an ideal gas equation of state,

$$p_k = (\gamma_k - 1)\rho_k e_k, \tag{9}$$

$$T_k = \frac{e_k}{c_{v,k}}, \tag{10}$$

$$h_k = \gamma_k e_k, \tag{11}$$

where $c_{v,k}$ is the specific heat at constant volume and γ_k is the ratio of specific heats for component k. An assumption of pressure and temperature equilibrium between the species allows an iterative process to be used to solve for component volume fractions, v_k. This, in turn, allows the determination of partial densities and energies according to

$$\rho_k = \frac{Y_k \rho}{v_k}, \tag{12}$$

TABLE I. Parameters used for the artificial transport terms in Eq. (19).

ψ_a	C_ψ	F	ϕ
μ_a	1.0×10^{-4}	$\frac{\rho}{\Delta}$	u_i
β_a	7.0×10^{-2}	ρ	$\frac{\partial u_i}{\partial x_i}$
κ_a	1.0×10^{-3}	$\frac{\rho}{T\Delta t}c_v$	T
$D_{a,\alpha}$	1.0×10^{-2}	$\frac{1}{\Delta t}$	Y_k

$$e = \frac{E}{\rho} - \frac{1}{2}u_i u_i = \sum_{k=1}^{N} Y_k e_k. \tag{13}$$

Total pressure is then calculated according to the mixture relationship

$$p = \sum_{k=1}^{N} v_k p_k. \tag{14}$$

These governing equations are solved using a tenth-order compact finite differencing scheme in space, and a fourth-order explicit Runge-Kutta scheme in time. Miranda has seen extensive use in compressible, multicomponent turbulent mixing problems [15,17–26]. The subgrid transfer of energy is modeling using an artificial fluid LES (AFLES) approach in which artificial transport terms are added to the fluid viscosity, bulk viscosity, thermal conductivity, and molecular diffusivity [13,14]. These are added according to

$$\mu = \mu_f + \mu_a, \tag{15}$$

$$\beta = \beta_f + \beta_a, \tag{16}$$

$$\kappa = \kappa_f + \kappa_a, \tag{17}$$

$$D_\alpha = D_{f,\alpha} + D_{a,\alpha}, \tag{18}$$

where the subscript f denotes the molecular contribution to the property from the fluid, and subscript a denotes the artificial contribution. As the present study is focused on the high-Reynolds number regime, the approach of Olson *et al.* [21] is adopted and the fluid contributions to each of these parameters is neglected, $\mu_f = \beta_f = \kappa_f = D_{f,\alpha} \equiv 0$. The artificial contribution to these terms are computed according to the method described by Campos and Morgan [25] as well as Morgan *et al.* [17]. Each of these terms has a functional form according to

$$\psi_a = C_\psi \overline{F G(\phi) \Delta^2}, \tag{19}$$

where ψ is the artificial fluid property, C_ψ is a tuning coefficient, $\Delta = (\Delta x \Delta y \Delta z)^{1/3}$ is the local grid spacing, and G is an eighth-order derivative such that for a scalar

$$G(\phi) = \max\left(\left| \frac{\partial^8 \phi}{\partial x^8} \Delta x^8 \right|, \left| \frac{\partial^8 \phi}{\partial y^8} \Delta y^8 \right|, \left| \frac{\partial^8 \phi}{\partial z^8} \Delta z^8 \right| \right) \tag{20}$$

and for a vector

$$G(\vec{\phi}) = \max(G(\phi_x), G(\phi_y), G(\phi_z)). \tag{21}$$

The overbar indicates the application of a truncated-Gaussian filter. The values of each of the tuning parameters, as well as F and ϕ, for each artificial component are outlined in Table I, where c_v is the

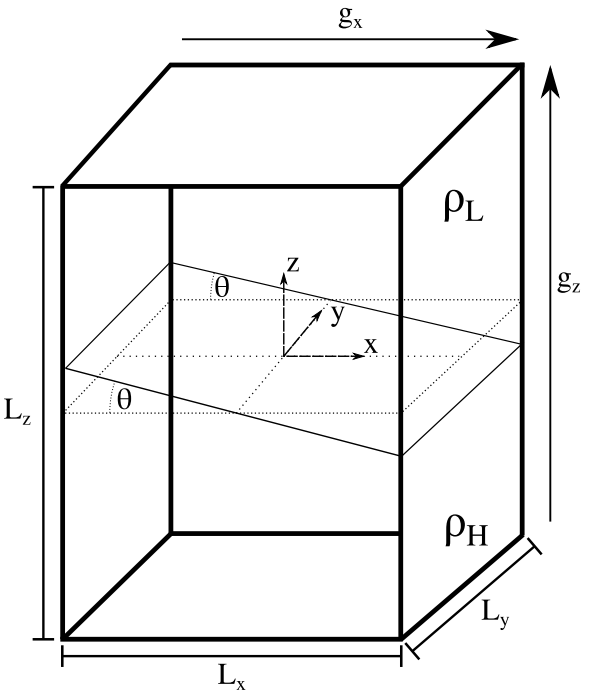

FIG. 2. Schematic representation of the problem domain. Dashed plane is located at the vertical midpoint of the domain, and the dashed lines are similarly located at the midpoints of the x and y axis.

specific heat at constant volume of the fluid and Δt is the time step. This form of the artificial terms is chosen to ensure that the artificial terms are biased towards the high-wave-number components of the flow and to have very low influence at resolved scales [13,19,25].

III. PROBLEM SETUP

A. Domain configuration

The configuration used in the present study aims to be similar to the Tilted Rocket Rig simulation of Andrews *et al.* [7] and closely follows case 110 from the experiments of Smeeton and Youngs [1]. The computational domain is depicted schematically in Fig. 2. In this figure, L_x, L_y, and L_z are the length of the computational domain in the x, y, and z axis, θ is the initial tilt angle of the interface relative to the horizontal, g_x and g_z are the applied acceleration in the x and z axis, and ρ_H and ρ_L are the densities of the heavy and light fluids, respectively. The triad indicates the location of $(x, y, z) = (0, 0, 0)$. The imposed boundary conditions are nonpenetrating for the left and right ($x = \pm 7.5$ cm) and top and bottom ($z = \pm 12.5$ cm) surfaces, with periodic boundary conditions on the front and back ($y = \pm 7.5$ cm) surfaces. One deviation from the experimental configuration is the expansion of the depth (L_y) of the domain from 2.5 cm in the experiment to 15 cm in the simulation. This was done to provide better converged statistical measurements for the quantities, which are averaged through the depth of the tank. This results in a simulation domain of 15 cm $\times$ 15 cm $\times$ 25 cm.

Simulations were run with several resolutions in order to assess mesh convergence. These mesh configurations are summarized in Table II. Each resolution is named R_N, where N is an integer multiplication factor that is applied to the zone counts at the coarsest mesh in order to arrive at the number of zones for higher resolution meshes. The zone counts in each axis at the coarsest mesh are chosen to ensure uniform grid spacing in all axes. The use of the multiplication factor to arrive

TABLE II. Simulation resolutions used for this study. All resolutions are integer multiples of the number of zones used in the coarsest simulation. The name for each resolution is R_N, where N is the multiplication factor used to arrive at the zone count for that resolution. N_x, N_y, and N_z are the number of zones in the x, y, and z axis, with N_{tot} representing the total zone count for the mesh. dx, dy, and dz are the grid spacing in x, y, and z.

Resolution name	N_x	N_y	N_z	N_{tot}	dx [cm]	dy [cm]	dz [cm]
R_1	66	66	110	479 160	0.227	0.227	0.227
R_2	132	132	220	3 833 280	0.113	0.113	0.113
R_4	264	264	440	30 666 240	0.057	0.057	0.057
R_8	528	528	880	245 329 920	0.028	0.028	0.028
R_{12}	792	792	1320	827 988 480	0.019	0.019	0.019
R_{16}	1056	1056	1760	1 962 639 360	0.014	0.014	0.014

at the zone counts for higher resolution meshes ensures that uniform grid spacing is maintained for all meshes.

B. Initial conditions

The fluids in this simulated problem are sodium iodide (NaI) and hexane (C_6H_{14}), chosen to match those used in case 110 of Smeeton and Youngs [1]. These fluids have densities of $\rho_H = 1.89$ g/cm^3 and $\rho_L = 0.66$ g/cm^3, respectively. This results in an Atwood number of

$$A = \frac{\rho_H - \rho_L}{\rho_H + \rho_L} = 0.4824.$$

The initial interface is located such that its mean location is centered in the domain. The interface has a tilt of $\theta = 5.766^\circ$ clockwise about the y axis, with this value having been chosen to match the experiment [1]. The initial interface perturbations in the experiment, particularly the high mode content, were not well characterized. Previous work has shown that RT simulations utilizing only very short wavelength perturbations will tend to underestimate typical observed mixing rates by approximately a factor of two [7,27–29]. The form of the broadband perturbation used in the present study was suggested by Andrews *et al.* [7] and has been shown previously to result in mixing rates similar to those observed in experiment [7]. Initial perturbations are prescribed as a superposition of modes using a power spectrum of the same form as described in [7],

$$P(k) \sim k^{-2},$$

where

$$k = \sqrt{k_x^2 + k_y^2}$$

is the two-dimensional wave number, with k_x and k_y are written as

$$k_i = \frac{2\pi}{\lambda_i} = \frac{2\pi N_i}{L_i},$$

where k_i is the wave number corresponding to a wavelength λ_i of a perturbation in the ith dimension. This can be equivalently stated using the mode number N_i, corresponding to a wave number with N periods in the ith dimension with length L_i. Here $N_{\min} = 2$ and $N_{\max} = 60$, which corresponds to $\lambda_{\max} = L_x/2 = 7.5$ cm and $\lambda_{\min} = 0.25$ cm. The power function is defined such that

$$\sigma^2 = \int_{k_{\min}}^{k_{\max}} P(k)\, dk,$$

where σ is the standard deviation with the value $\sigma = 0.001\lambda_{\max}$. The height, z_{int}, of the initial interface with center position $(x, y, z) = (0, 0, 0)$ is calculated as a function of horizontal position (x, y) according to

$$z_{\text{int}}(x, y) = \tan(\theta)x + \sum_{N_x}\sum_{N_y} T(x)\sqrt{P(k)}\cos\left(\frac{2\pi N_x}{L_x}x + \phi_x\right)\cos\left(\frac{2\pi N_y}{L_y}y + \phi_y\right), \tag{22}$$

where N_x, N_y are in the range $N_{\min} \leqslant N \leqslant N_{\max}$, $T(x)$ is a Tukey window with a half-width of 1.5 cm applied to the perturbations near the left and right boundaries, and ϕ_i are uniformly distributed random phase offsets in the range $(0, 2\pi]$. The values of ϕ are calculated for each unique pair of N_x and N_y. That is to say, a fixed value of N_x does not have the same value of ϕ_x when varying N_y. This is similarly true for the case of N_y when varying N_x. The random number generator used to generate these random phases is seeded with a fixed value prior to generation of the interface profile to ensure that the perturbations are identical between runs.

The high-order numerics used by Miranda necessitate that flow variables change value smoothly across the interface so as to avoid introducing nonphysical Gibbs' oscillations. This smooth transition in flow variables across the interface is accomplished by specifying an initial diffusion thickness of the interface. The initial diffusion profile is specified using a weighting function with the form of a hyperbolic tangent function oriented normal to the unperturbed interface location, which is calculated as follows: For a given position (x, y, z) in the simulation domain, the nearest point located on the interface is determined by the intersection of a line normal to the mean (unperturbed) interface profile that passes through the point (x, y, z) with the perturbed interface profile. This intersection point is (x^i, y^i, z^i). The weighting function is then calculated according to

$$\mathcal{W}(x, y, z) = \frac{1}{2}\left\{\tanh\left[\text{sgn}[z - z_{\text{int}}(x, y)]\frac{\sqrt{(x - x^i)^2 + (y - y^i)^2 + (z - z^i)^2}}{s}\right] + 1\right\}, \tag{23}$$

where sgn is the sign function, and s is a stretching factor to control the width of the diffusion profile. A value of $s = 5dz/4$ was chosen for this work, resulting in a diffusion width of approximately five cells. $\mathcal{W}$ varies between 0 below the interface to 1 above it. A function of this form ensures that the initial diffusion profile is oriented normal to the initial interface profile. The function $\mathcal{W}$ is then used to generate an initial condition which varies smoothly across the interface between the two fluids. For example, for a quantity Q with constant values Q_H below the interface and Q_L above the interface, a field with a smooth transition between the two values across the interface is calculated according to

$$Q(x, y, z) = Q_H + (Q_L - Q_H)\mathcal{W}(x, y, z), \tag{24}$$

where Q may be any quantity which is expected to vary smoothly across the interface, such as density or species mass fraction.

The acceleration profile for the Tilted Rocket Rig problem may be specified in one of two ways. One option is to use the acceleration time history from the experiment itself. The acceleration profile from the experiment is reproduced in Fig. 3 with data from Andrews *et al.* [7]. However, the acceleration profile from the experiment is time-varying with rapid changes in the acceleration applied to the fluids, and as a result this approach can cause problems for compressible codes, such as Miranda, with regard to nonphysical density excursions or the formation of shock waves [7]. An alternative approach used here is to specify a constant acceleration together with a matching hydrostatic pressure gradient. An equivalent constant acceleration value was derived in [7] using the bubble growth model of Layzer [30] together with the limiting bubble and spike velocities of Goncharov [31]. This results in an equivalent constant acceleration parallel to the z axis of $g = 3.5 \times 10^{-8}$ cm/μs^2. The details of how this equivalent acceleration is derived, and the establishment of a nondimensional timescale that relates the time varying and constant gravity cases, is discussed in greater detail in Sec. III D. An additional constant component of acceleration

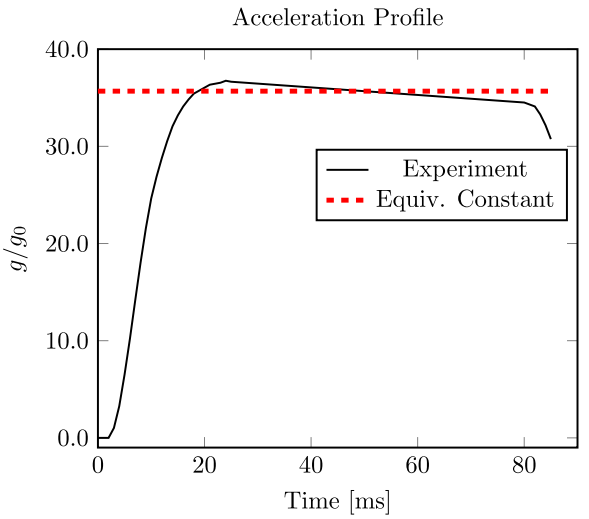

FIG. 3. Acceleration history of the experiment, reproduced using data from Andrews *et al.* [7], compared with constant acceleration used in the present work.

from the tilt of the tank is applied along the x axis, $g_x = g_0 \sin(\theta)$, where g_0 is Earth's gravity, 9.81×10^{-10} cm/μs^2.

The hydrostatic gradient which results from the application of the constant acceleration is applied to the domain according to

$$P(x, y, z) = \rho_H g_z \left[\min(z, z_{\text{int}}(x, y)) - \left(-\frac{L_z}{2} \right) \right] + \rho_L g_z [\max(z, z_{\text{int}}(x, y)) - z_{\text{int}}(x, y)] + P_0, \quad (25)$$

where $z_{\text{int}}(x, y)$ is the height of the interface in the column of fluid at (x, y). The pressure is specified with a value of $P_0 = 20$ bar at the bottom of the tank, with this value having been chosen to reduce the influence of compressibility [7]. It should be noted that this form of the pressure assumes an infinitely sharp interface, while the true interface is diffuse. This assumption is true in the limit of the highest resolutions of the problem, and no significant disturbance to the pressure field as a result of this initial pressure field is observed at any resolution.

C. Averaging

Several forms of averaging are utilized in the analysis presented in this work. The first operation which will be used is the Reynolds decomposition, written as

$$f = \bar{f} + f', \quad (26)$$

where $\bar{f}$ is the unweighted average of f, and f' is the fluctuations of f about this average. A second decomposition which will be used in this work is Favre, or mass-weighted, averaging. This is defined as

$$\widetilde{f} = \frac{\overline{\rho f}}{\bar{\rho}} \quad (27)$$

such that f may be alternatively decomposed as

$$f = \widetilde{f} + f'', \quad (28)$$

where $\widetilde{f}$ is the Favre-averaged value of f, and f'' is the fluctuations of f about this average. In both cases, these averaging operations are assumed to be through the depth (y) of the tank.

A final form of averaging concerns vertical lineouts that will be presented as part of this work. When considering lineouts considered as part of this work, two averaging operations are undertaken. The first is to average the data through the depth (y) of the tank. This reduces the three-dimensional (x, y, z) data to two-dimensional data (x, z). Second, the middle 40% of the x axis of the domain is selected in order to exclude the influence of the sidewall bubble and spike plumes. A lineout is taken in each column (z) of this subselected data. Each of these lineouts is then offset using the tilt angle of the interface and the x position of the column of data to remove the influence of the interface tilt on the average profile. The method used to calculate the interface tilt angle will be described in Sec. IV A 3. Each of these shifted lineouts is then averaged together to calculate a single average one-dimensional lineout of the quantity of interest. This type of averaging is denoted with angle brackets, and referred to as a tilt-compensated average profile. In other words, $\langle \bar{f} \rangle$ denotes the value of f which has been first averaged through the depth of the tank using Reynolds averaging, and then averaged along the middle 40% of the x axis.

D. Nondimensionalization

It is useful to introduce quantities which will be used to nondimensionalize the quantities presented in this work. In all cases in this work, a symbol with a superscript asterisk ($*$) denotes the nondimensionalized form of a variable. f^*, for instance, represents the nondimensionalized form of a quantity f.

Utilizing a constant acceleration in place of the time-varying acceleration from the experiment requires a suitable nondimensionalization to make results comparable between the two cases. Andrews *et al.* [7] specifies a nondimensional time, τ, as

$$\tau = \int_0^t \sqrt{\frac{Ag(t)}{L_x}}\, dt + \delta, \tag{29}$$

where $A = (\rho_2 - \rho_1)/(\rho_2 + \rho_1)$ is the Atwood number, g is the (not necessarily constant) gravity, L_x is the width of the simulation domain, and δ is a correction factor. This correction factor was found by Andrews *et al.* [7] by considering the bubble growth model of Layzer [30] together with the terminal bubble and spike velocities of Goncharov [31]. These model equations can be solved while considering a case with time varying gravity as well as a case with constant gravity. Andrews *et al.* performed this analysis with parameters representative of the bulk overturning motion of this flow. They find that for a constant acceleration of $g = 3.5 \times 10^{-8}$ cm/μs^2, the predicted bubble and spike heights versus nondimensional time τ lie on top of each other when an offset of $\delta = -0.053$ is applied to the variable gravity case. For further detail on this analysis, the reader is referred to [7]. The predicted bubble and spike heights from the time-varying and constant acceleration cases are plotted in terms of this nondimensional time in Fig. 4. This analysis gives confidence that the present constant acceleration simulation is comparable to the variable acceleration experiment, as well as to variable acceleration simulations, when treated using this relationship. Given that the present work considers the constant gravity case, the square root term in Eq. (29) may be removed from the integral. Noting that this term has units of inverse time, a characteristic timescale, t_0, is specified as

$$t_0 = \sqrt{\frac{L_x}{Ag}} \tag{30}$$

such that the nondimensional time may be written as $t^* = t/t_0$. Note that $t^* = \tau$ in the constant gravity case. The simulation is run out to $t = 60$ ms, corresponding to $t^* = 2.01$. This is approximately the time that the upwards-traveling spike of heavy fluid on the left edge of the domain reaches the top of the simulation domain.

The definition of t^* given by Andrews *et al.* [7] was arrived at utilizing the bubble growth model of Layzer [30] combined with the limiting bubble and spike velocities of Goncharov [31]. As a

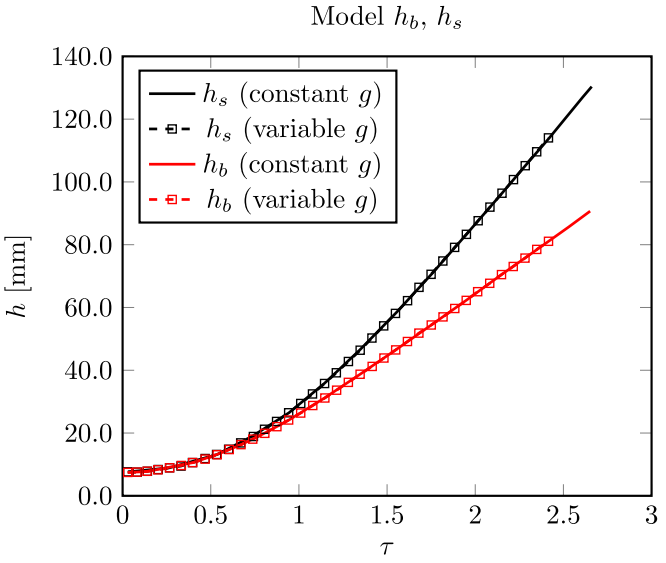

FIG. 4. Predicted bubble and spike growth for the constant and variable acceleration cases (from Andrews *et al.* [7]) plotted vs nondimensional time, τ [Eq. (29)], for each case over the window of time simulated in this work.

result, a characteristic velocity scale equivalent to the limiting bubble velocity of Goncharov [31] is utilized, which is defined as

$$u_0 = \sqrt{\frac{2A}{1+A}\frac{g}{3\bar{k}}} \tag{31}$$

such that $u^* = u/u_0$, where A is the Atwood number, g is the gravity, and $\bar{k}$ is the perturbation wave number, here chosen as the centroid of the initial perturbation spectrum,

$$\bar{k} = \frac{1}{\frac{1}{k_{\text{min}}} - \frac{1}{k_{\text{max}}}} \ln\left(\frac{k_{\text{max}}}{k_{\text{min}}}\right). \tag{32}$$

These time and velocity scales are then used to define a characteristic length scale as

$$\ell_0 = u_0 t_0 = \sqrt{\frac{2Ag}{3\bar{k}(1+A)}}\sqrt{\frac{L_x}{Ag}} = \sqrt{\frac{2L_x}{3\bar{k}(1+A)}} \tag{33}$$

such that $\ell^* = L/\ell_0$.

IV. RESULTS: GRID CONVERGENCE AND DATA COMPARISONS

A. Temporal convergence

The quantities of interest in this section are the temporal trends of the height of the sidewall bubble and spike plumes, the integral mixed width, the interface tilt angle (θ), the global mixing parameter (Θ), and the average value of turbulent kinetic energy. These quantities are examined for their trends over time, as well as how these trends change with increasing grid resolution. Figure 5 is an annotated version of the experimental image at $t = 59.8$ ms from Fig. 1 and is useful to establish the physical representation of some of these quantities. This figure depicts the line corresponding to $y = 0$ in this work, the mean interface location and corresponding tilt angle, θ, as well as the dimensions corresponding to the sidewall bubble (h_b) and spike (h_s) heights.

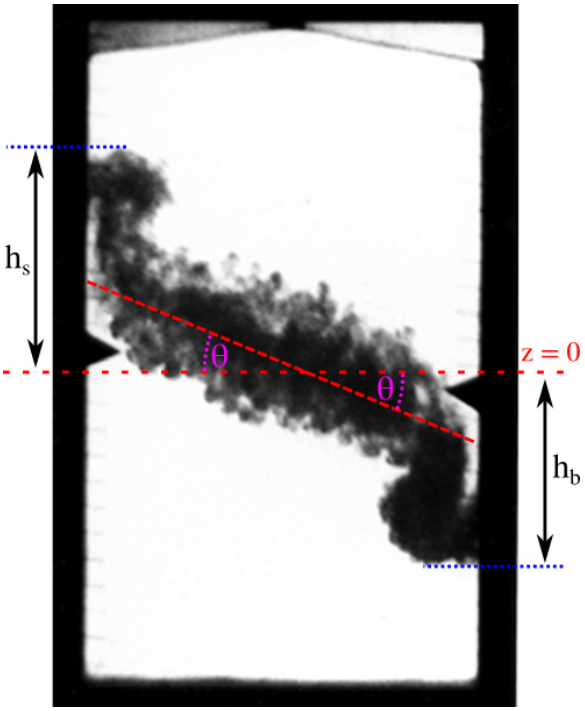

FIG. 5. Annotated version of the experimental image at $t = 59.8$ ms from Fig. 1. Indicated is the line corresponding to $y = 0$ in this simulation, the mean interface location, the interface tilt angle, θ, and the dimensions corresponding to the sidewall bubble (h_b) and spike (h_s) heights.

1. Bubble and spike height

The height of the bubble and spikes is calculated by first taking the planar average of the heavy fluid mass fraction to get a profile of average heavy mass fraction versus the vertical (z) coordinate:

$$\langle Y_H \rangle(z) = \frac{1}{L_x}\frac{1}{L_y}\int_x \int_y Y_H(x, y, z)\, dx\, dy, \tag{34}$$

where Y_H is the mass fraction of the heavy fluid, and L_x and L_y are the width and depth of the tank, respectively. The crossings of 0.1% and 99.9% average heavy mass fraction are then identified as the location of the spike and bubble, respectively. A plot of the bubble and spike heights versus time, together with experimental data and the $600 \times 600 \times 960$ mesh TURMOIL results of Andrews *et al.* [7], is presented in Fig. 6. Note that while the criteria used to identify the bubble and spike heights used in this work match the criteria of [7], the experimental measurements of Smeeton and Youngs [1] were based on photographic analysis of the experimental images which utilized light refraction based on density fluctuations. While the data from these two methods are comparable, this difference in analysis should be acknowledged. Good agreement with the TURMOIL results is observed for the highest resolution simulations in the present work. It is noted that these simulations generally overpredict the bubble and spike heights versus the experimental data, particularly at later times. This trend was also observed in the TURMOIL data. The difference between the experimental data and simulation results is attributed to the different acceleration profiles (time-varying versus constant) between the experiment and simulation. Additional analysis has been conducted which also examines the influence of the choice of this threshold value on the resulting values of h_b and h_s. This analysis is presented in the Appendix. The general conclusion is that the values of h_b and h_s do show a slight sensitivity to the choice of threshold used, and thresholds which may

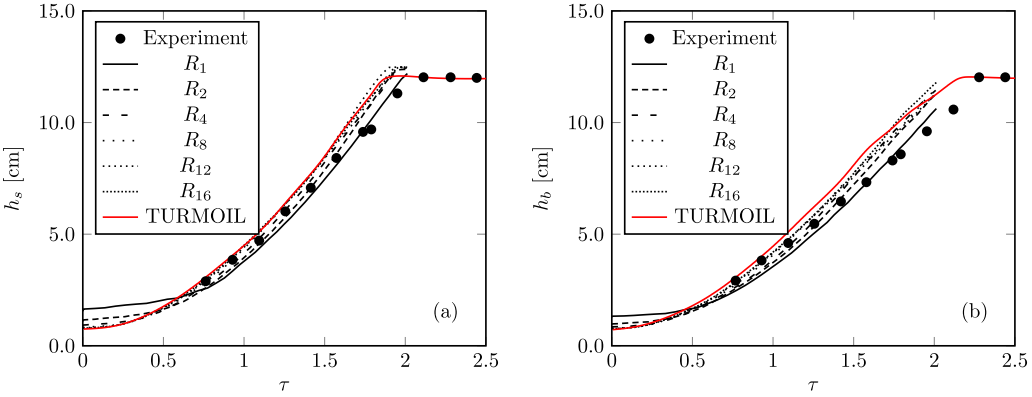

FIG. 6. Heights of the (a) rising spike of heavy fluid on the left side of the domain and (b) falling bubble of light fluid on the right side of the domain. Experimental data from Smeeton and Youngs [1] (reproduced from Andrews *et al.* [7]) are presented for comparison. TURMOIL data are taken from the $600 \times 600 \times 960$ mesh results of [7]. Note that the data are plotted vs τ [Eq. 29)] for comparison purposes. The leveling off of the bubble and spike heights at the latest times is attributed to the interaction of the sidewall bubble and spikes with the bottom and top of the domain, respectively.

be more representative of those used in the experiment do demonstrate better early to mid-time agreement with the experimental data. However, the later time disagreement between the experiment and simulation is still observed.

Generally, increasing resolution appears to cause the height of the sidewall bubble and spike plumes to increase for a fixed instant in time. This change may, in part, be influenced by the decrease in the initial diffusion thickness rather than being solely an effect of increased grid resolution. Notably, while decreases in initial diffusion thickness do appear to increase the values of h_b and h_s at a fixed time, this effect is less pronounced for each subsequent refinement of the computational grid, and good convergence of the sidewall bubble and spike heights is observed at the highest resolutions.

Finally, a leveling off of the spike height at the latest times for the highest resolution simulations from the present work is also observed, which is attributed to the rising plume of heavy fluid beginning to interact with the upper boundary of the domain. This leveling-off behavior is also observed in bubble and spike heights of the experiment and TURMOIL simulation at the latest times. The difference in the maximum bubble and spike heights attained between the present simulations and the experiment as well as TURMOIL data is attributed to the difference in vertical domain extents between the two cases (24 cm in experiment and TURMOIL [7], 25 cm in the present work).

2. Integral mix width

The integral mix width is another way that the width of the mixing layer may be calculated. This is defined as [32]

$$W = \frac{1}{L_x} \iint \bar{Y}_H \bar{Y}_L \, dx \, dz, \tag{35}$$

where $\bar{Y}_L$ and $\bar{Y}_H$ are the depth-averaged light and heavy mass fractions, respectively. It may also be noted that for this two-fluid problem, $Y_L = 1 - Y_H$. The value of integral mix width versus time and simulation resolution is presented in Fig. 7. There are two trends in the behavior of W with changing mesh resolution that are observed. First, there is a general decrease in W at early times with increasing mesh resolution. This is due to the decrease in the initial diffusion thickness with

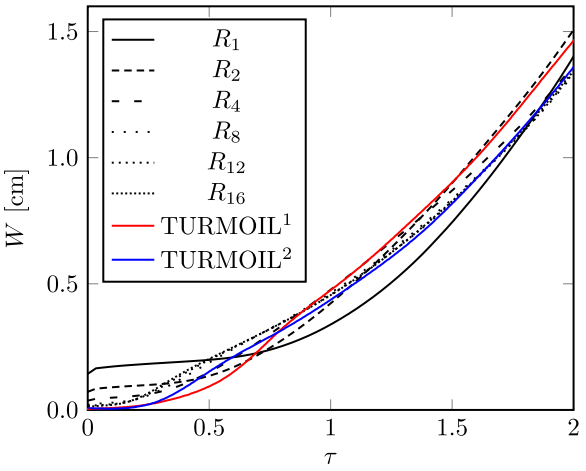

FIG. 7. Integral mixed width [Eq. (35)] vs time and simulation resolution. TURMOIL data are from the (1) $300 \times 300 \times 480$ and (2) $600 \times 600 \times 900$ meshes of Andrews *et al.* [7]. Note that the nondimensional time is τ [Eq. 29)] to facilitate comparison between constant and time-varying gravity simulations.

increasing mesh resolution. Second, the later time values of W are observed to increase from the R_1 to R_2 mesh but then decrease with increasing mesh resolution beyond this point. This is attributed to the improved resolution of the initial perturbation spectrum with additional mesh refinement and an associated change in the physics of the problem. On the R_1 mesh, the initial perturbation spectrum is not fully resolved, and the modes that are resolved are generally similar to, or smaller than, the initial diffusion thickness, reducing their growth and the degree of self-interaction that takes place. On the R_2 mesh, a greater number of modes are resolved, and the largest, long-wavelength modes become comparable in amplitude to the diffusion thickness, while the short-wavelength modes remain small compared to the diffusion thickness, mitigating their influence. This results in the mixing layer effectively consisting primarily of low mode components which grow fairly large before self-interacting, resulting in a greater value of W as compared to the R_1 mesh. Then, beginning with the R_4 mesh, an increasing fraction of the shorter-wavelength, small-amplitude perturbations become large compared to the grid spacing and diffusion thickness, increasing their influence on the flow. This results in an increased degree of self-interaction at earlier times in the simulation, in turn resulting in a decreased integral mixing layer width. Further refinement to the mesh results in a greater fraction of the high-wave-number, low-amplitude modes being resolved, further increasing self-interaction at earlier times and decreasing the value of W. Refining to the R_8 mesh and beyond shows relatively little change to the value or trend of W over time, with the results from the R_8 through R_{16} meshes lying nearly on top of each other in Fig. 7, indicating the solution is well converged at the highest resolutions. Good agreement with the $600 \times 600 \times 900$ mesh TURMOIL results of Andrews *et al.* [7] is also observed at the highest resolutions in the present study.

3. Interface tilt angle

The interface undergoes a bulk overturning motion as the mixing layer evolves in time, resulting in a increasing tilt angle of the interface with time. This is indicated by θ in Fig. 5. The tilt angle of the interface may be calculated as a function time by a least-squares fit to the mean interface location over the middle 40% of the domain. The mean interface location is found as a function of the horizontal (x) coordinate according to

$$h(x) = \int_{-L_z/2}^{L_z/2} \bar{Y}_H(x, z)\, dz. \tag{36}$$

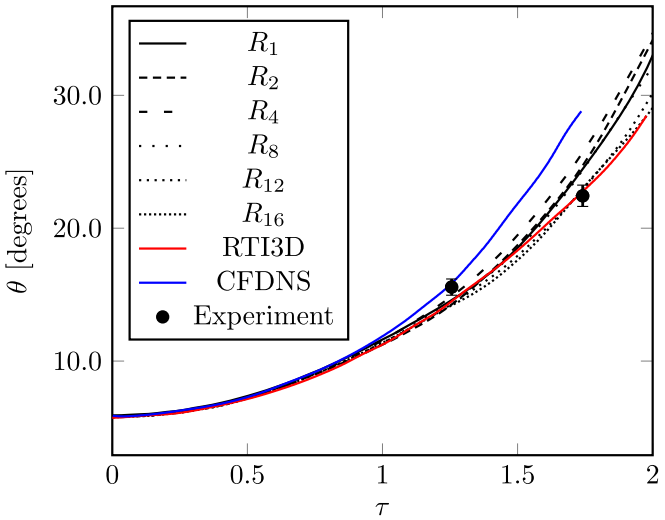

FIG. 8. Interface tilt angle vs time and resolution. RTI3D and CFDNS data are from Andrews *et al.* [7]. The RTI3D data are from the $512 \times 512 \times 768$ simulation, and CFDNS data are from the $\mathrm{Re} = 14000$ simulation. Experimental data are found by estimating the tilt angle using the images in Fig. 1. Note that τ [Eq. (29)] is used for nondimensional time to facilitate comparison between constant gravity and time-varying gravity simulations.

The interface tilt angle versus time and resolution is presented in Fig. 8. Also included are two tilt angles from the experiment corresponding to the images in Fig. 1(a) and Fig. 1(b). These angles were estimated by using imaging-processing software to analyze the middle 40% of the image. The location of the top and bottom of the mixing layer are found by searching for the location of the 90% image intensity crossings. The location of the middle of the mixing layer is picked to be the location of the minimum image intensity. Linear fits to these three estimations are used to estimate the slope, and therefore the tilt angle, of the mixing layer. The average of these three tilt angle estimates is used to estimate the overall tilt angle of the mixing layer. The uncertainty in these estimations arises from the uncertainty of the fits. It should be emphasized that these angles are only estimates based on analysis of these published images and are not obtained from the original experimental data. Good agreement between all resolutions is observed up until $t^* \approx 1.2$, at which point the trend of interface tilt angle versus time deviates slightly with changing resolution. An initial increase in the interface tilt angle at the latest times is observed from R_1 to R_2, and again from R_2 to R_4. R_8 and R_{12} demonstrate a decrease in the interface tilt angle with increasing resolution at the latest times. R_{12} and R_{16} have similar trends through time, indicating this metric is well converged for the highest resolution runs. These results also demonstrate good agreement with the RTI3D results of Andrews *et al.* [7] at the highest grid resolutions. Additionally, good agreement with the estimated experimental data is also observed.

4. Global mixing parameter

The global mixing parameter is a measure of the amount of mixed fluid versus the amount of entrained fluid and is defined according to

$$\Theta = \frac{\int \overline{Y_L Y_H}\, dx\, dz}{\int \bar{Y}_L \bar{Y}_H\, dx\, dz}. \tag{37}$$

The value of Θ ranges from 0, representing a state where all fluid is entrained and none is mixed, to 1, representing a state where all fluid is mixed. A plot of Θ versus time and simulation resolution is shown in Fig. 9. A general trend where there is an increased amount of entrained fluid at early times

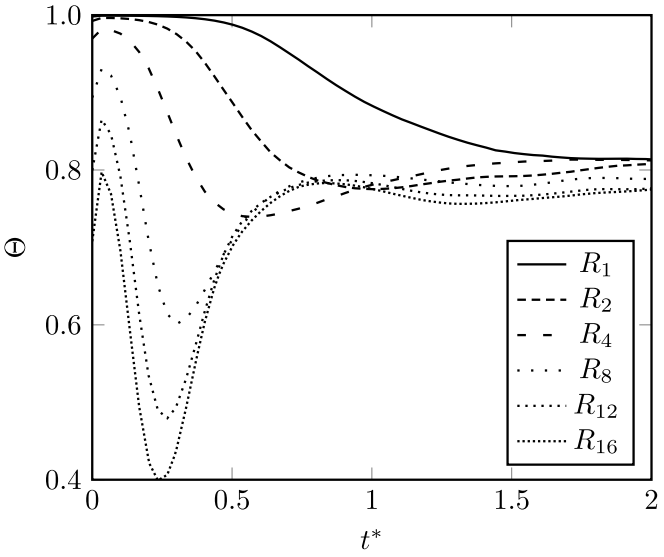

FIG. 9. Global mixing parameter vs nondimensional time and grid resolution.

in the simulation is observed with increasing resolution. The lowest resolution runs, $R_{N\leqslant 4}$, do not appear to achieve a turbulent transition, indicated by the lack of a decrease and subsequent increase in Θ. Higher resolution runs do appear to achieve a turbulent transition, with an approximately asymptotic value of $\Theta \approx 0.78$ attained at late times. The late-time convergence of Θ for $R_{N\geqslant 8}$ indicates that these simulations have achieved a fully turbulent mixing layer with mixing which resembles planar RTI configurations. In particular, these simulations are in good agreement for $t^* \geqslant 1$, which will be the focus for subsequent investigation in this work.

5. Turbulent kinetic energy

The Favre-averaged Reynolds stress tensor is given by

$$\widetilde{R}_{ij} = \frac{\overline{\rho u_i'' u_j''}}{\bar{\rho}}. \tag{38}$$

Therefore the turbulent kinetic energy (TKE) is

$$\widetilde{\mathrm{TKE}} = \frac{1}{2}\mathrm{Tr}(\widetilde{R}_{ij}) = \frac{1}{2}\widetilde{R}_{ii} = \frac{1}{2}\frac{\overline{\rho u_i'' u_i''}}{\bar{\rho}}, \tag{39}$$

and the total amount of TKE in the domain is then

$$k_{\mathrm{tot}} = L_y \iint \bar{\rho}\widetilde{\mathrm{TKE}}\, dx\, dz. \tag{40}$$

Figure 10 depicts the total amount of turbulent kinetic energy in the tank versus time and simulation resolution. The TKE results from the $512 \times 512 \times 768$ inviscid (RTI3D-I) and viscous (RTI3D-V) ILES simulations of Denissen *et al.* [8] are included for comparison. A marked increase in turbulent kinetic energy is observed in the transition from R_1 to R_2. This may be attributed to the spectrum of the initial perturbations not being fully resolved at the coarsest simulation resolution together with a diffuse interface, both of which act to diminish the amount of small-scale flow motions that are created. The increase in resolution from R_1 to R_2 allows a greater fraction of the initial interface perturbations to be resolved in the sense of being >1 grid cell in height, and the interface becomes less diffuse, resulting in an increase in overall TKE. Further increases in

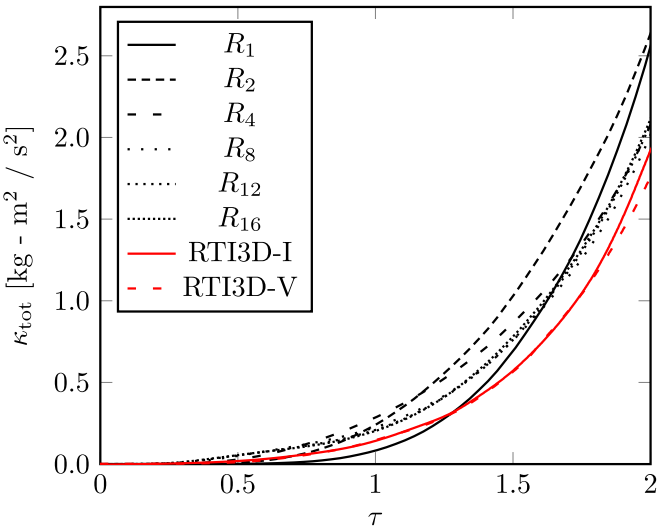

FIG. 10. Total amount of turbulent kinetic energy vs time and resolution. RTI3D data taken from the 512×512×768 simulations of Denissen *et al.* [8]. RTI3D-I and RTI3D-V refer to inviscid and viscous ILES simulations, respectively. Note that data are plotted vs τ [Eq. (29)] to facilitate comparison between constant and time-varying gravity simulations.

resolution then demonstrate a decrease in the total amount of TKE at a fixed time versus the lower resolution runs. This is initially counterintuitive but is attributed to a change in the underlying physics of the problem. Recall that the width of the initial diffusion profile is a function of grid size. Therefore, most of the high-wave-number modes present on the interface will be smaller than one grid cell, and much smaller than the diffusion thickness, particularly at low grid resolutions. This has the effect of "washing out" the higher wave-number contributions (with correspondingly low amplitudes) of the initial spectrum at low resolutions. This causes the bubble and spike growth to more closely follow that of a single mode interface, manifesting as increased TKE due to the larger velocity values attained before interaction between modes takes place. Increasing resolution reduces the width of this initial diffusion zone, allowing the higher wave-number components to be better resolved. This causes a greater degree of self-interaction between modes, with this interaction occurring at earlier times. This in turn reduces the amplitude of the velocity fluctuations, resulting in an apparent decrease in TKE despite an increase in the number of modes present. Little change in the amount of TKE is expected once these perturbations are fully resolved, and indeed this is what is observed. This behavior is also consistent with the results shown in Fig. 7, where changes in integral mixed width with increasing grid resolution are attributed to changes in the interaction of the spikes and bubbles in the central mixing layer. Likewise, the plot of global mixedness in Fig. 9 suggests that R_1 through R_4 do not attain a turbulent transition, which also indicates the lack of self-interaction between modes. Overall, the highest resolution runs are all well converged in integrated TKE, with a small change observed between R_4 and R_8, and almost no change observed from R_8 to R_{16}. The present simulations demonstrate a slightly greater amount of TKE than is observed in the ILES simulations of Denissen *et al.* [8], but otherwise agree well. The difference between these two cases is attributed to differences in the numerical method utilized as well as the influence of different grid spacing between the two simulations.

B. Spatial convergence

The previous sections have demonstrated that the simulations presented here have achieved good convergence with respect to temporal trends of the solution. It is also useful to examine the trends

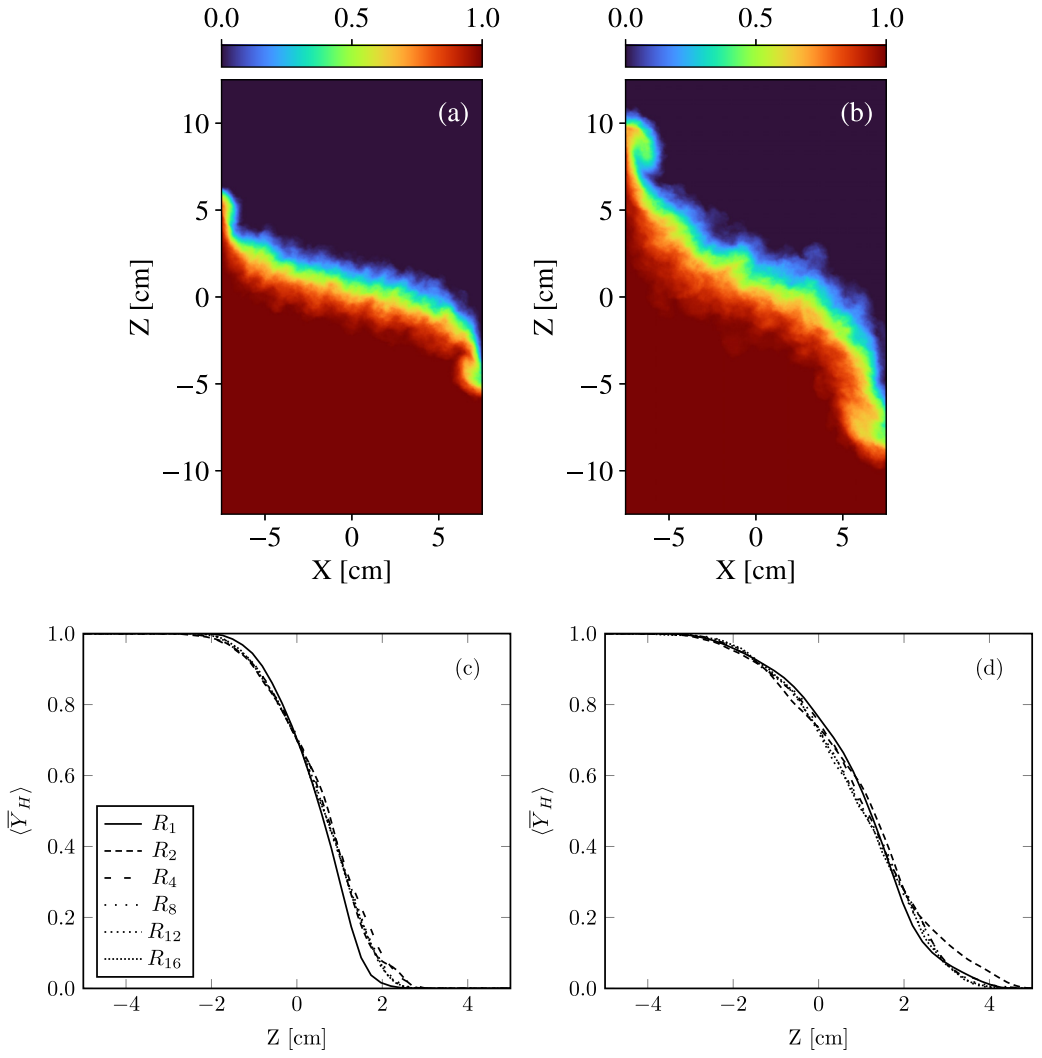

FIG. 11. Pseudocolor of depth-averaged heavy mass fraction from the R_{16} mesh run and tilt-compensated average profiles for each simulation resolution at two time instances: (a), (c) $t^* = 1.241$ and (b), (d) $t^* = 1.745$.

of spatial profiles at a fixed time to ensure that convergence with respect to spatial variations has also been achieved.

1. Heavy mass fraction

Pseudocolor plots of $\bar{Y}_H$ from the highest resolution simulation at $t^* = 1.241$ and $t^* = 1.745$ are presented in the top half of Fig. 11. The bottom half of this figure depicts the average profile of $\bar{Y}_H$ for each simulation resolution run as part of this study. A slight shift in the tilt-compensated average profile is observed from R_1 to R_2. This can be attributed to the additional grid points more completely resolving the initial perturbation spectrum. Increasing resolution beyond this point does not show a significant change with regard to this averaged profile, demonstrating good convergence at the highest resolution runs.

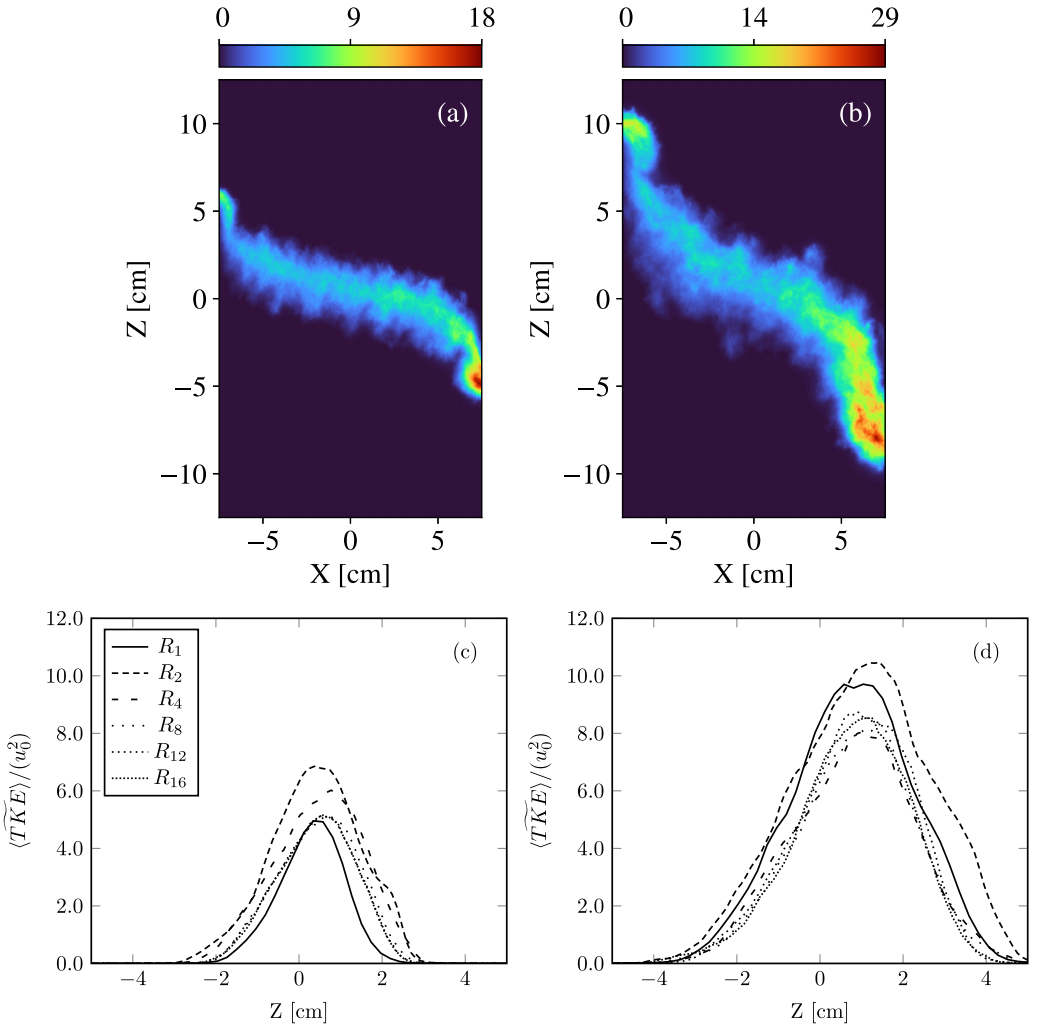

FIG. 12. Pseudocolor of depth-averaged normalized turbulent kinetic energy, $\mathrm{TKE}^* = \widetilde{\mathrm{TKE}}/u_0^2$, from the R_{16} mesh run and corresponding tilt-compensated profiles for each simulation resolution at two time instances: (a, c) $t^* = 1.241$ and (b, d) $t^* = 1.745$.

2. Turbulent kinetic energy

The depth-averaged distribution of turbulent kinetic energy for the highest simulation resolution as well as the spatially averaged profile of turbulent kinetic energy for all resolutions are presented in Fig. 12 for two time instances, $t^* = 1.241$ and $t^* = 1.745$. TKE is fairly uniformly distributed across the domain, though more intense regions of TKE are observed in tip of the falling bubble on the right-hand side of the domain. A second, less intense peak in the spatial distribution of TKE is observed at the tip of the rising spike on the left-hand side of the domain. The tilt-compensated average profile of TKE has an approximately Gaussian shape, with the peak intensity of TKE located at the center of the mixing layer. The change of the spatial profile of TKE with changing resolution is similar to the change in temporal trends of TKE with increasing resolution observed in Fig. 10. At early times, a large increase in TKE is observed from when going from R_1 to R_2. This may be attributed to the initial perturbation spectrum being more fully resolved by the increased resolution. Additional resolution increases result in a decrease in the magnitude of TKE across the mixing

layer, although the spatial distribution remains relatively similar. This trend is similar at later times with the exception that the jump in TKE between the two lowest resolutions is not observed. This trend of decreasing TKE with increasing simulation resolution was also observed in the temporal trends of TKE in Fig. 10. As with the temporal trends, this behavior is attributed to better resolving the highest mode contributions with increasing grid resolution.

V. RESULTS: TURBULENT TRANSPORT BUDGETS

Having built confidence in our results by demonstrating solution convergence as well as favorable comparison with prior works in the previous section, we now seek to more fully characterize mass and momentum transport by considering the spatial distributions and turbulent budgets of turbulent mass flux velocity, species transport, species variance, and Reynolds stresses. This section examines the results in two ways. First, two-dimensional depth-averaged plots of the flow variables of interest will be presented at two time instances corresponding to $t^* = 1.241$ ($t = 37$ ms) and $t^* = 1.745$ ($t = 52$ ms). Second, vertical lineouts of the terms in the unclosed budget equations for each flow variable of interest are presented. These lineouts are calculated similarly to the procedure described for the spatially averaged profiles in Sec. III C, with the note that the budget equations used here are all already depth-averaged, and so do not require any additional averaging in that axis.

Several budget equations examined as part of this work include the species mass fraction of species α, Y_α. Analysis in these cases will be restricted only to the heavy fluid, $\alpha = H$, without loss of information due to the fact that this is a two-fluid problem. The results for the light fluid, $\alpha = L$, may be found from the heavy fluid results by noting that $Y_L = 1 - Y_H$. Additionally, terms in the budget equations which include neglected molecular transport quantities (D_f, μ_f, etc.) are themselves neglected in this analysis.

A. Turbulent mass flux velocity

1. Distribution

The first quantity of interest is the value of the turbulent mass flux velocity, which is defined as [33]

$$a_i = -\overline{u_i''} = \frac{\overline{\rho' u_i'}}{\bar{\rho}}, \tag{41}$$

where u_i is the velocity in axis i, ρ is the density, and a_i is the turbulent mass flux velocity corresponding to velocity component i. This term represents the transport of mass due to turbulent velocity in the mixing layer and is an important source of production of TKE in buoyancy driven flows. Two-dimensional pseudocolor plots depicting the spatial distribution of $a_i^* = a_i/u_0$ at $t^* = 1.241$ and $t^* = 1.745$ are shown in Fig. 13. Several trends may be observed in these distributions. For the horizontal component [Figs. 13(a) and 13(c)], there is a transport of mass that is opposite of the density gradient between the two fluids. This is localized to the central mixing layer and increases in intensity over time. This countergradient flux behavior has also been observed in other work on this problem [8]. In the vertical axis, a general upwards transport of mass is observed, with the greatest turbulent mass flux velocity located in the spike and bubble plumes. Additionally, the magnitude of a_z^* is approximately five times greater than that of a_x^* along the centerline.

Another way to visualize the transport of mass shown in Fig. 13 is to use a quiver plot, with the components of a_i as the components of the vector. A separate run on the R_4 mesh with an initial tilt angle of $\theta = 20^\circ$ was conducted. This greater tilt angle was chosen in order to reduce the disparity between the horizontal and vertical components of a_i to make the direction of mass transport easier to visualize. This is presented in Fig. 14, where $a_i = \{a_x, a_z\}$. The main plot depicts a_i over the region where $0.1 \leqslant \bar{Y}_H \leqslant 0.9$ at $t^* = 1.0$. The inset depicts a zoomed-in region depicting the mixing layer in more detail. The contour lines depict $\bar{Y}_H$ from 0.1 to 0.9 in steps of 0.1. Examination of the inset plot reveals that the transport of mass is upwards and to the right from below the mixing layer. This transport of mass then turns upwards and to the left as it transits the interface and reaches the light side of the mixing layer.

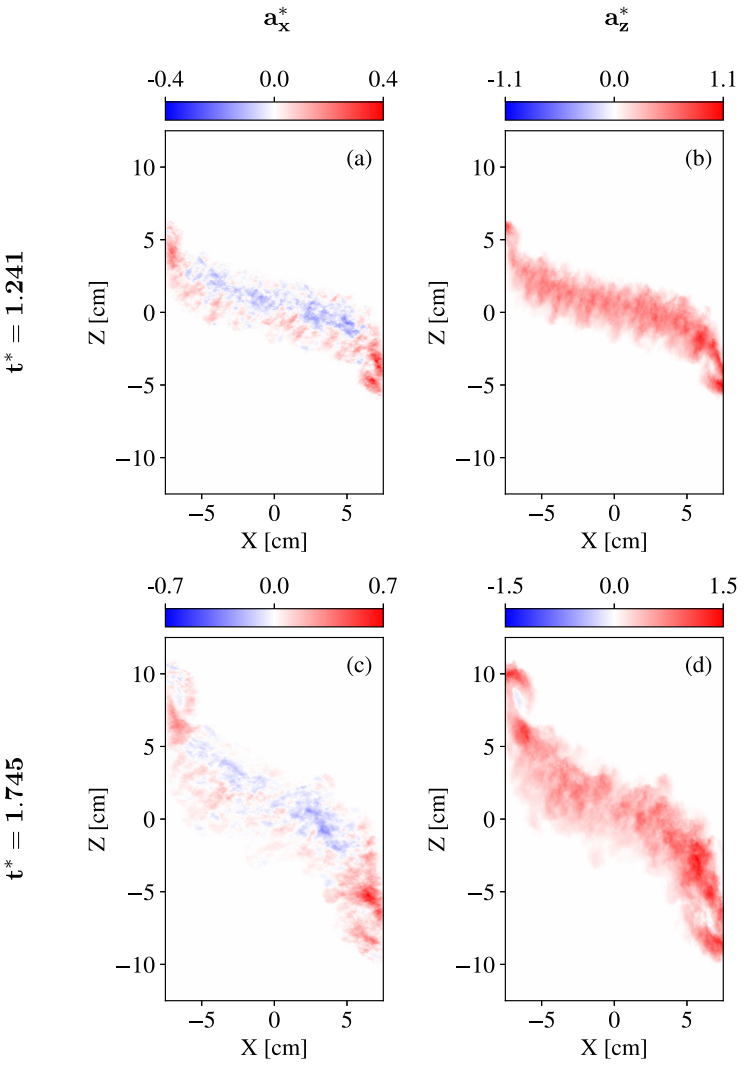

FIG. 13. Distribution of (left) a_x^* and (right) a_z^* at (top) $t^* = 1.241$ and (bottom) $t^* = 1.745$.

2. Budget equation

The transport equation for turbulent mass flux velocity, given by Besnard *et al.* [33] and reproduced from Wong *et al.* [34], is

$$\underbrace{\frac{\partial(\bar{\rho}a_i)}{\partial t}}_{\text{Term1}} + \underbrace{\frac{\partial(\bar{\rho}\tilde{u}_k a_i)}{\partial x_k}}_{\text{Term2}} = \underbrace{b\left(\frac{\partial \bar{p}}{\partial x_i} - \frac{\partial \bar{\tau}_{ki}}{\partial x_k}\right)}_{\text{Term3a}} - \underbrace{\tilde{R}_{ik}\frac{\partial \bar{\rho}}{\partial x_k}}_{\text{Term3b}} + \underbrace{\bar{\rho}\frac{\partial(a_k a_i)}{\partial x_k}}_{\text{Term4a}} - \underbrace{\bar{\rho}a_k\frac{\partial \bar{u}_i}{\partial x_k}}_{\text{Term4b}} - \underbrace{\bar{\rho}\frac{\partial(\overline{\rho' u_i' u_k'}/\bar{\rho})}{\partial x_k}}_{\text{Term5}}$$
$$+ \underbrace{\overline{\bar{\rho}\left(\frac{1}{\rho}\right)'\left(\frac{\partial p'}{\partial x_i} - \frac{\partial \tau_{ik}'}{\partial x_k}\right)'} - \bar{\rho}\overline{u_i'\frac{\partial u_k'}{\partial x_k}}}_{\text{Term6}}, \tag{42}$$

where b is the density-specific volume covariance, $b = -\overline{\rho'(1/\rho)'}$. Term 1 represents the time rate of change, term 2 represents convection, term 3 represents production, term 4 represents

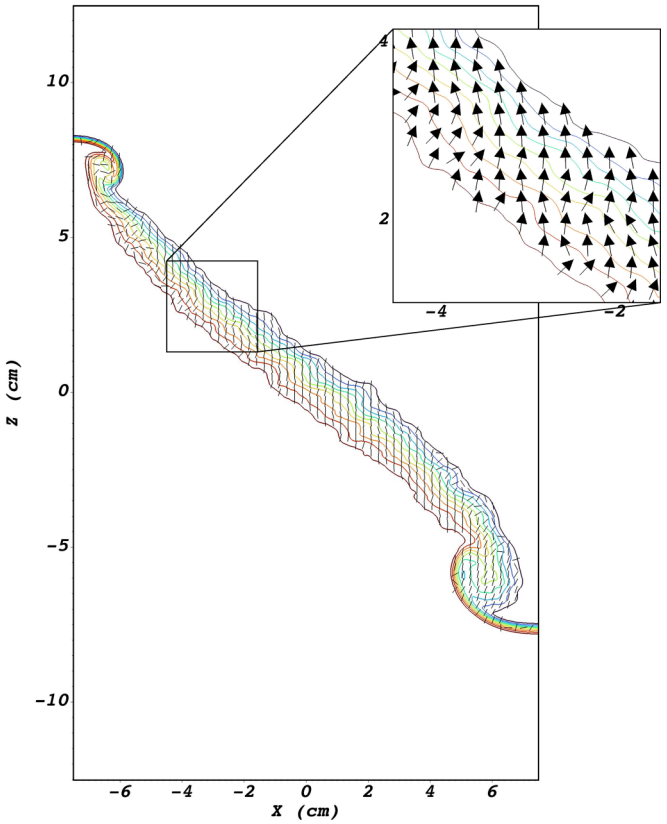

FIG. 14. Quiver plot of $a_i = \{a_x, a_z\}$. Transport of mass normal to the interface and then leftward is visible in the inset.

redistribution, term 5 represents turbulent transport, and term 6 represents destruction. Note that term 3 has been split into term 3a and 3b, with these representing production due to buoyancy and Reynolds stress, respectively. Similarly, term 4 has been split into terms 4a and 4b, representing redistribution due to correlation between axes and due to flow gradients. Figure 15 depicts each budget term averaged over the center of the domain at $t^* = 1.241$ and $t^* = 1.745$. The dominant contributions to the budget equation in the horizontal axis (x) come from terms 4 and 6. Similarly, the dominant contributions to the budget equation in the vertical axis (z) are from terms 3 and 6. This indicates, perhaps unsurprisingly, that the transport most aligned with gravity is dominated by production and destruction, while the transverse component is primarily influenced by redistribution and destruction. Figure 16 presents terms 3 and 4 broken into terms a and b for each axis. The most significant contribution in the vertical (z) axis is from the production terms, which are approximately equally split between the buoyancy (term 3a) and Reynolds stress (term 3b) production. The most significant contribution in the horizontal (x) axis is from the redistribution term, which is dominated by term 4b. This term is frequently neglected in RANS models such as K-L-a [35]. The present results suggest that it is necessary to include this term to accurately predict two-dimensional mixing.

Further analysis of the budget terms in Fig. 16 demonstrates a few other trends worthy of note. In the horizontal axis, the combined production term (term 3) has a semi-sinusoidal shape. The split of this term reveals that this occurs due to the contribution of term 3b, representing production via Reynolds stress, as term 3a demonstrates a single-sided parabolic profile. A similar behavior is observed in the vertical component of the combined redistribution term (term 4). The pseudo-

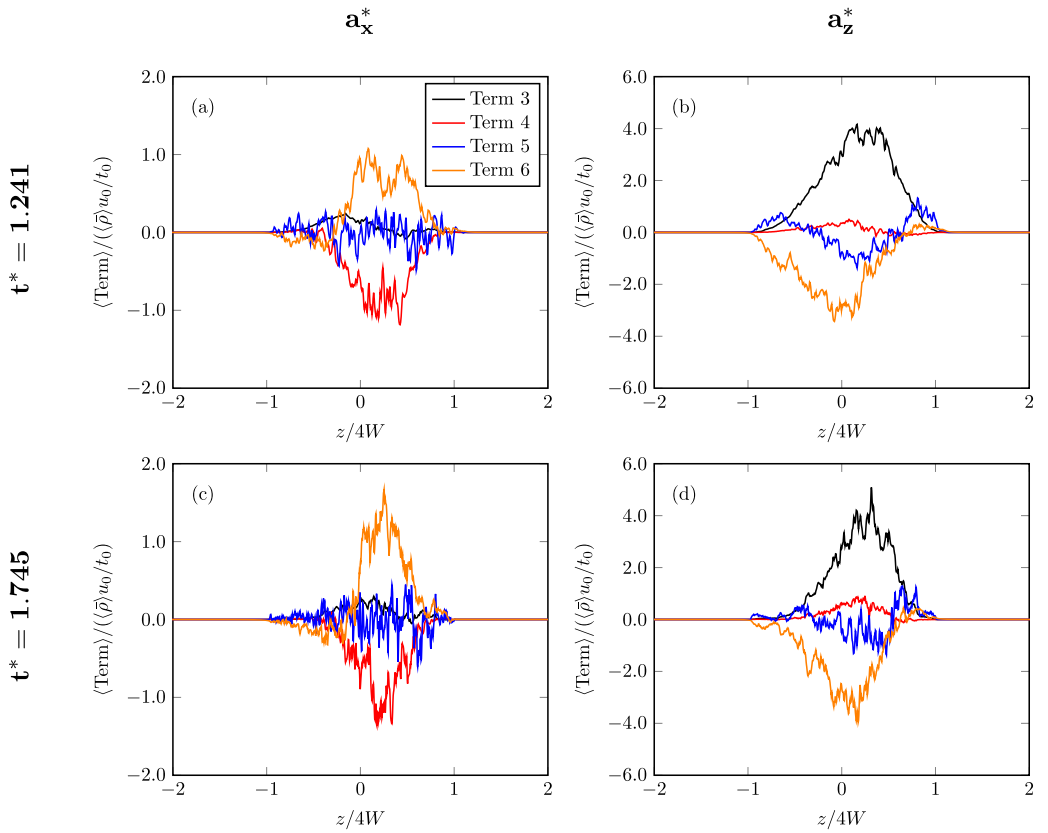

FIG. 15. Terms of the turbulent mass flux budget [Eq. (42)] in (left) the horizontal (x) axis and (right) the vertical (z) axis at (top) $t^* = 1.241$ and (bottom) $t^* = 1.745$.

sinusoidal shape of this term is due to the influence of term 4a, representing correlation between axes, as term 4b, representing the influence of flow gradients, is single-sided. In both cases, these terms are not the dominant contribution to the budget equations in their respective axes.

B. Species mass fraction flux

The species mass fraction flux is defined as [36]

$$\Omega_i^\alpha = Y_\alpha'' u_i'' \quad \therefore \widetilde{\Omega}_i^\alpha = -\frac{\overline{\rho Y_\alpha'' u_i''}}{\bar{\rho}}. \tag{43}$$

Note the negative sign in the definition of $\widetilde{\Omega}_i^\alpha$. This was added in keeping with the definition of Braun and Gore [36]. Figure 17 depicts the distribution of $\widetilde{\Omega}_i^{\alpha *} = \widetilde{\Omega}_i^\alpha / u_0$ at $t^* = 1.241$ and $t^* = 1.745$. A strong similarity between the species mass fraction flux and the distribution of turbulent mass flux velocity (Fig. 13) is observed, both in the qualitative distribution of each quantity as well as in the range of values attained by each metric. As a consequence, similar observations may be made. A countergradient flux of horizontal species mass fraction is observed on the light fluid side of the central mixing layer. The intensity of this countergradient flux increases over time. The vertical transport of the heavy species mass fraction is likewise similar to the vertical component of the turbulent mass flux velocity distribution. A general upwards transport of the heavy fluid is observed across the mixing layer, with the most intense regions of upwards transport concentrated in the side-wall bubble and spike plumes.

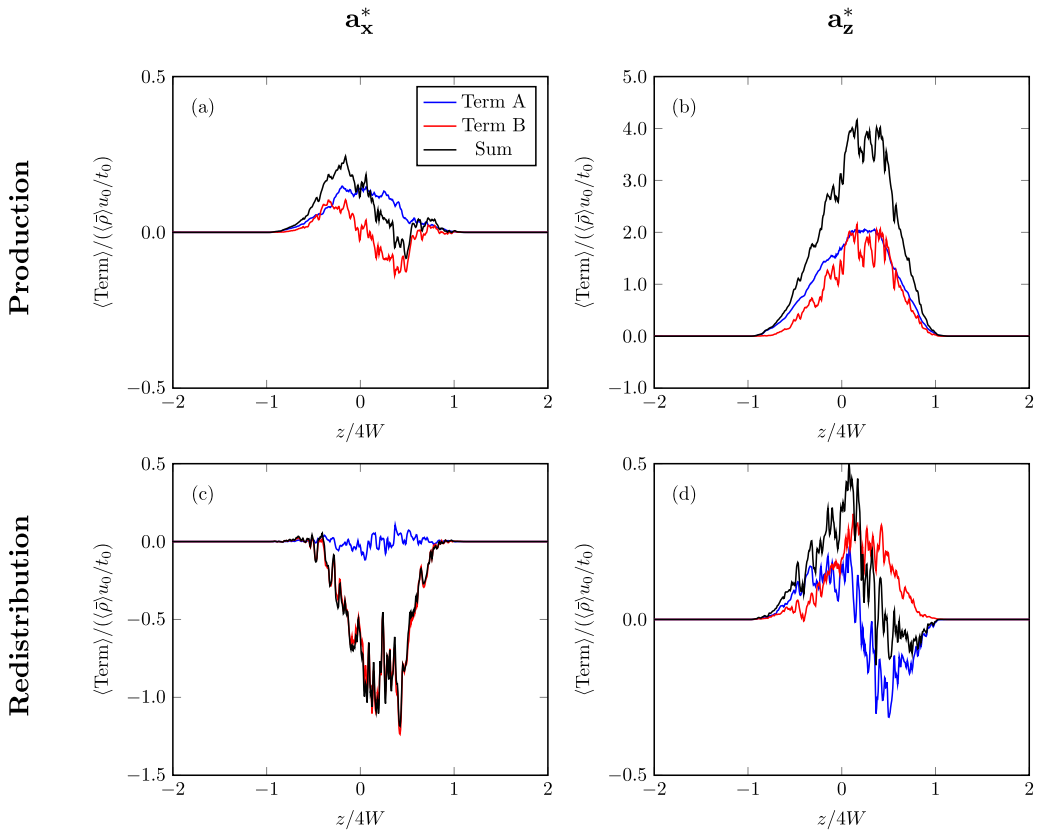

FIG. 16. Split contributions to the combined (top) production (term 3) and (bottom) redistribution (term 4) terms of the turbulent mass flux budget [Eq. (42)] in (left) the x axis and (right) the z axis. All plots are from $t^* = 1.241$.

1. Budget equation

The budget equation for species mass fraction flux is taken from Braun and Gore [36], and with some rearrangement is stated as

$$\underbrace{\frac{\partial \bar{\rho}\widetilde{\Omega}_i^\alpha}{\partial t}}_{\text{term 1}} + \underbrace{\frac{\partial\left(\bar{\rho}\widetilde{\Omega}_i^\alpha\right)}{\partial x_j}}_{\text{term 2}} = \underbrace{\overline{Y_\alpha''}\frac{\partial \bar{P}}{\partial x_i}}_{\text{term 3a}} + \underbrace{\bar{\rho}\widetilde{R}_{ij}\frac{\partial \widetilde{Y}_\alpha}{\partial x_j}}_{\text{term 3b}} + \underbrace{a_i\frac{\partial\left(\bar{\rho}\widetilde{\Omega}_j^\alpha\right)}{\partial x_j}}_{\text{term 4a}} - \underbrace{\bar{\rho}\widetilde{\Omega}_i^\alpha\frac{\partial \bar{u}_i}{\partial x_j}}_{\text{term 4b}}$$
$$+ \underbrace{\frac{\partial(\overline{\rho u_i' u_j'' Y_\alpha''})}{\partial x_j}}_{\text{term 5}} - \underbrace{\overline{Y_\alpha''\frac{\partial \sigma_{in}'}{\partial x_n}} - \overline{u_i''\Delta^{\alpha'}}}_{\text{term 6}}, \tag{44}$$

where a_i is the turbulent mass flux velocity [Eq. (41)], $\sigma_{ij} = \tau_{ij} - \delta_{ij}\bar{P}$ and δ_{ij} is the Kronecker delta, and $\Delta^{\alpha'} = D_{j,j}^\alpha - \rho\overline{D_{j,j}^\alpha}/\bar{\rho}$. This has been arranged to approximately correspond to the labeled terms in the budget for turbulent mass flux velocity. Term 1 is the time rate of change, term 2 is transport, term 3a, and term 3b correspond to production, term 4a and 4b represent redistribution, term 5 represents turbulent transport, and term 6 represents destruction. Note that in this work $D_f \equiv 0$, and so terms containing $\Delta^{k'}$ are neglected. Recalling that $\mu_f \equiv 0$ for this work, we find that terms containing σ_{ij}' may also be neglected. This, in effect, results in neglecting the entirety of term 6. Figure 18 shows the terms of this budget equation for components of Eq. (44) corresponding to

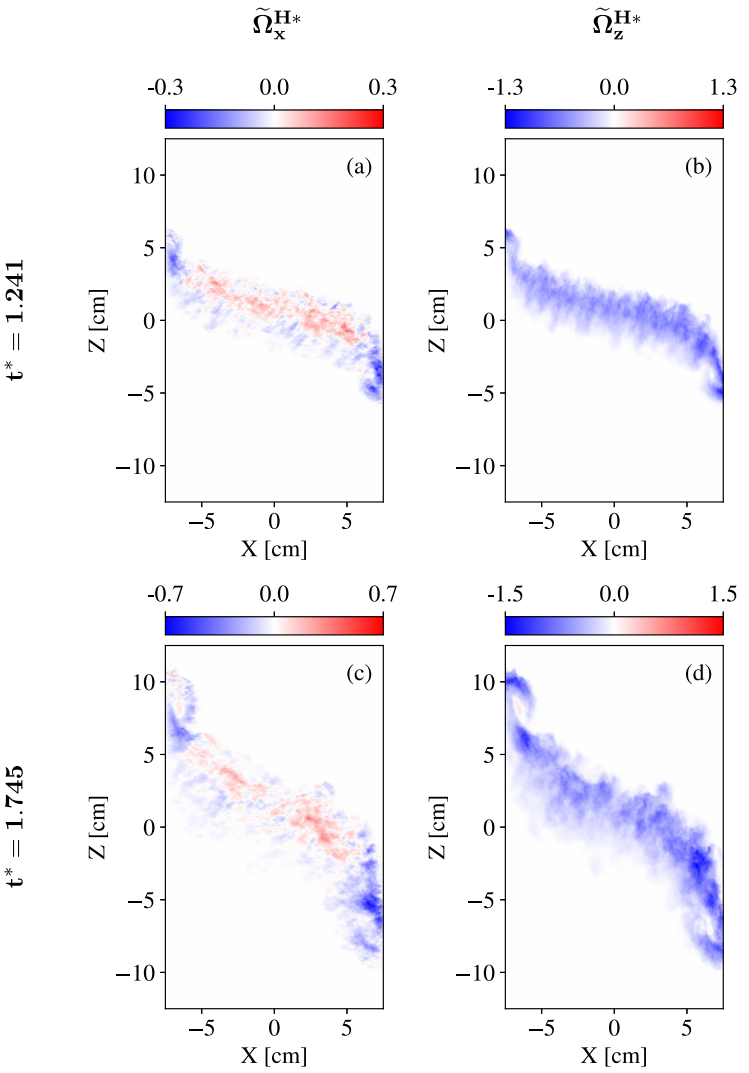

FIG. 17. Distribution of (left) $\widetilde{\Omega}_x^{H*}$ and (right) $\widetilde{\Omega}_z^{H*}$ at (top) $t^* = 1.241$ and (bottom) $t^* = 1.745$.

the horizontal and vertical components of velocity at times $t^* = 1.241$ and $t^* = 1.745$. Perhaps unsurprisingly given the similar spatial distributions of mass flux velocity and species mass fraction flux, similar trends to those observed for the budget of turbulent mass flux (Fig. 15) are observed here. The contributions to the budget equation in the horizontal axis are primarily dominated by the combined redistribution term (term 4). The vertical component of the budget equation is dominated by contributions from the combined production term (term 3). Also notable in the vertical axis is that term 5, representing turbulent transport, also has a non-negligible contribution. This contribution is negative on the edges of the mixing layer, and positive towards the center, representing a diffusive-like transport of species mass fraction flux.

The combined production (term 3) and redistribution (term 4) terms can once again be split into their "a" and "b" components. Figure 19 depicts these contributions to each term in each axis at $t^* = 1.241$. Similar observations as those made for the turbulent mass flux velocity budget terms can be made here. The combined production term (term 3) is the dominant term in the budget of $\widetilde{\Omega}_z^H$,

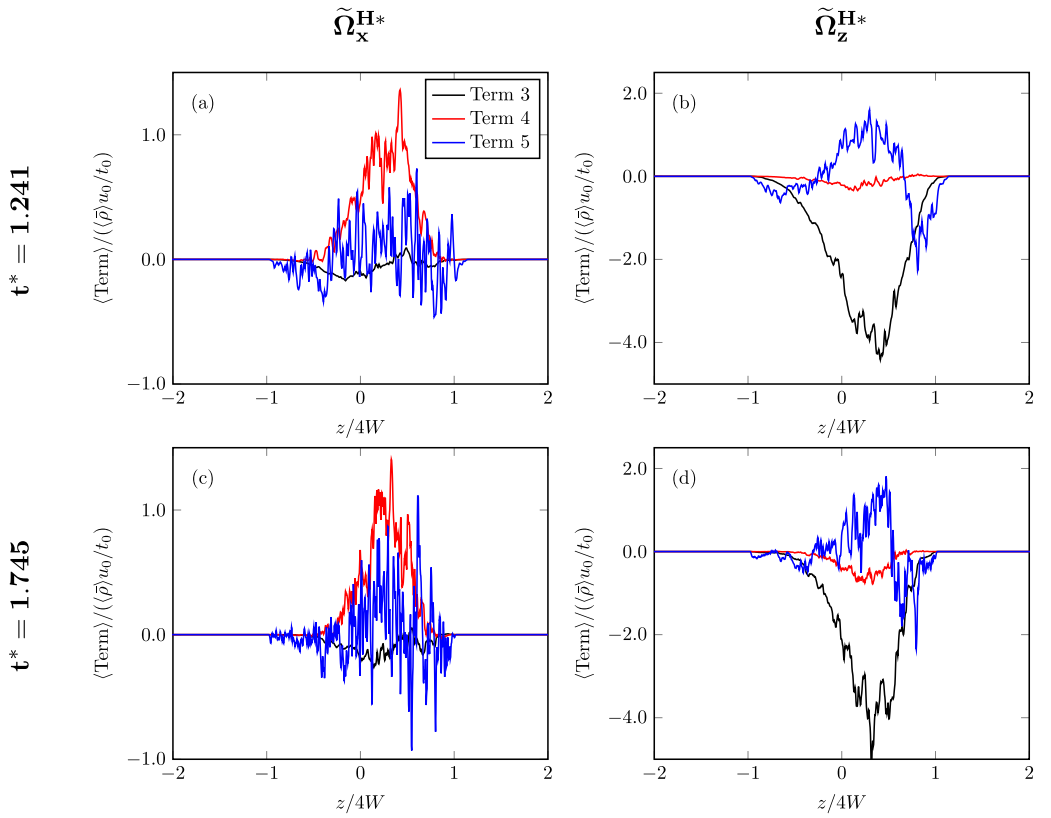

FIG. 18. Terms in the budget of species mass fraction flux [Eq. (44)] for (left) the horizontal axis and (right) the vertical axis at times (top) $t^* = 1.241$ and (bottom) $t^* = 1.745$.

and the two split production terms comprise approximately equal portions of the total. The combined redistribution term (term 4), which is the dominant term in the budget for $\widetilde{\Omega}_x^H$, is dominated by contributions from the "b" term. These trends are similar to the those observed for the budgets of the turbulent mass flux velocity, a_i. Additionally, term 3 in the horizontal axis has a pseudo-sinusoidal distribution, with a zero crossing near the central part of the mixing layer. Term 3a, representing buoyancy production, is single-sided, and so this behavior cannot be explained by that term alone. This behavior is caused by the contribution from term 3b, representing production from the Reynolds stress, which also changes sign around the middle of the mixing layer. This trend is also observed in the vertical component of term 4, though in this case both terms "a" and "b" change signs across the mixing layer, contributing to the sign change of the overall term. This is in contrast to the vertical component of term 4 from the turbulent mass flux velocity, where part "a" was single sided and only part "b" was responsible for the change in sign of this term across the mixing layer.

C. Scalar mass fraction variance

1. Spatial distribution

The scalar mass fraction variance is defined as

$$\widetilde{Y_\alpha''^2} = \frac{\overline{\rho Y_\alpha'' Y_\alpha''}}{\bar{\rho}} \tag{45}$$

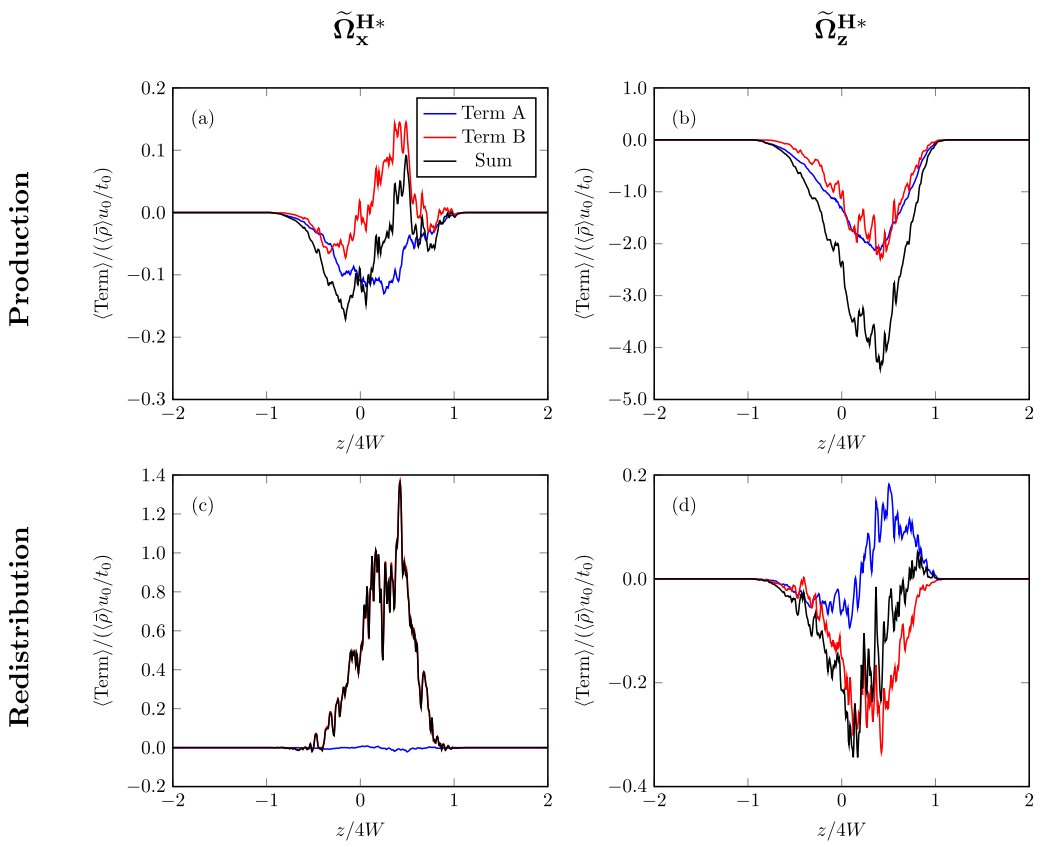

FIG. 19. Split contributions to the combined (top) production (term 3) and (bottom) redistribution (term 4) terms from the budget equation for species mass fraction flux [Eq. (44)] in the (left) horizontal and (right) vertical axis.

and will be referred to simply as "scalar variance" going forward. Recall that, as this is a two-fluid problem, only the heavy fluid ($\alpha = H$) will be considered here. Figure 20 depicts the distribution of $\widetilde{Y_H''^2}$ over the simulation domain at $t^* = 1.241$ and $t^* = 1.745$. The variance of heavy mass fraction is relatively evenly distributed horizontally over the mixing layer, with the greatest variance at the center of the layer, and decreasing variance towards the edges. A region of increased variance is observed near the edge of the domain, at the base of the spike of heavy fluid traveling up the side wall, as well as at the top of the mushroom structure at the tip of the plume. This behavior is particularly noticeable at later times. This increased variance is not observed near the root of the plume of light fluid on the right edge of the domain, however.

2. *Budget equation*

The budget equation for scalar mass fraction variance is [37]

$$\underbrace{\bar{\rho}\frac{\partial \widetilde{Y_\alpha''^2}}{\partial t}}_{\text{term 1}} + \underbrace{\bar{\rho}u_i\frac{\partial \widetilde{Y_\alpha''^2}}{\partial x_i}}_{\text{term 2}} = \underbrace{-2\overline{\rho u_i'' Y_\alpha''}\frac{\partial \widetilde{Y}_\alpha}{\partial x_i}}_{\text{term 3}} \underbrace{-2\overline{\rho D\frac{\partial Y_\alpha''}{\partial x_i}\frac{\partial Y_\alpha''}{\partial x_i}}}_{\text{term 4}} + \underbrace{\frac{\partial}{\partial x_i}\left(\overline{\rho D\frac{\partial Y_\alpha''^2}{\partial x_i}} - \overline{\rho u_i'' Y_\alpha''^2}\right)}_{\text{term 5}}, \tag{46}$$

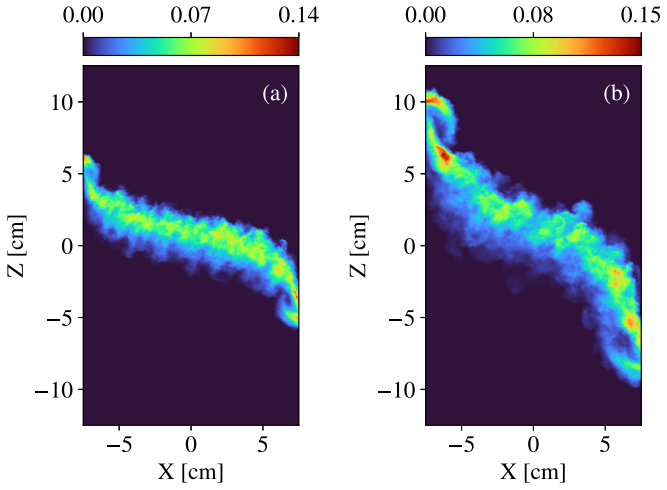

FIG. 20. Distribution of $\widetilde{Y_\alpha''^2}$ at (a) $t^* = 1.241$ and (b) $t^* = 1.745$.

where term 1 is the time rate of change, term 2 is the transport, term 3 is production, term 4 is dissipation, and term 5 is turbulent transport and diffusion. Note that term 4, as well as the first part of term 5, have been neglected as they contain D_f, which was taken to be zero for this study. Figure 21 depicts the budget terms at $t^* = 1.241$ and $t^* = 1.745$. These budget terms indicate that production of scalar variance is greatest in the center of the mixing layer. The turbulent transport of scalar variance is negative in the center of the mixing layer, and positive on the edges. This indicates a diffusive-like redistribution of variance from the center to the edges of the mixing layer.

D. Favre-averaged Reynolds stress tensor

1. Spatial distribution

The Favre-averaged Reynolds stress is defined as

$$\widetilde{R}_{ij} = \frac{\overline{\rho u_i'' u_j''}}{\bar{\rho}}. \tag{47}$$

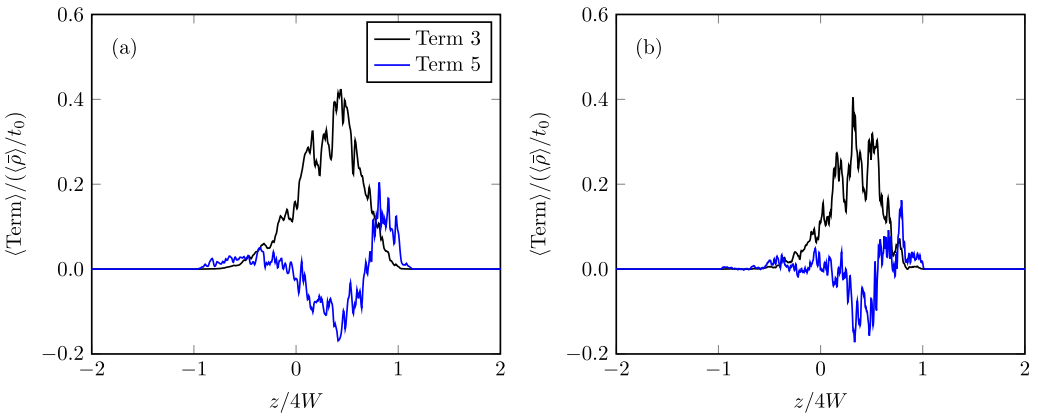

FIG. 21. Budget terms for scalar variance [Eq. (46)] at (a) $t^* = 1.241$ and (b) $t^* = 1.745$.

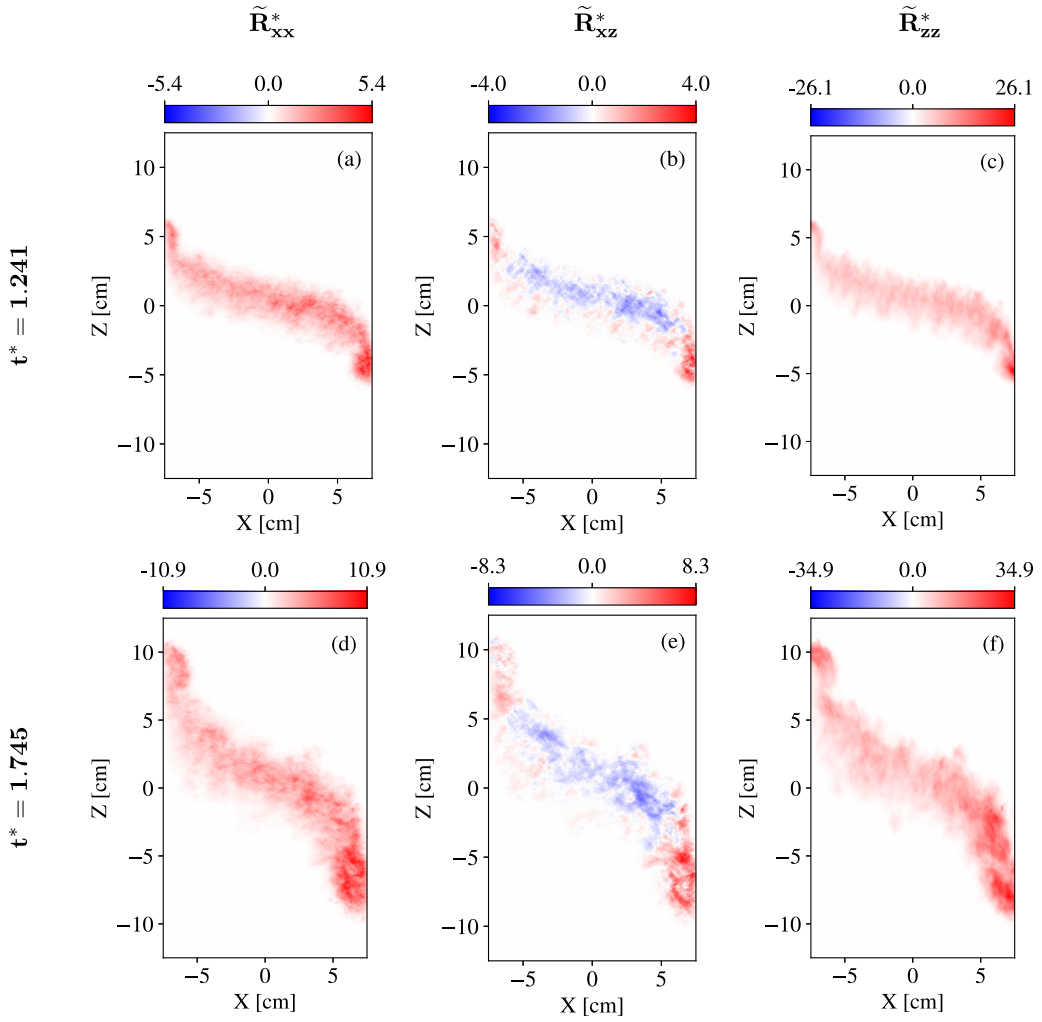

FIG. 22. The spatial distributions of (left) $\widetilde{R}^*_{xx}$, (center) $\widetilde{R}^*_{xz}$, and (right) $\widetilde{R}^*_{zz}$ at (top) $t^* = 1.241$ and (bottom) $t^* = 1.745$.

Only $\widetilde{R}_{xx}$, $\widetilde{R}_{xz}$, and $\widetilde{R}_{zz}$ are resolved in this work by noting that the simulation is periodic in y. The spatial distribution of the resolved components of $\widetilde{R}^*_{ij} = \widetilde{R}_{ij}/u_0^2$ at $t^* = 1.241$ and $t^* = 1.745$ is presented in Fig. 22. Qualitative similarities to the distributions of turbulent mass flux velocity (Fig. 13) and species mass fraction flux (Fig. 17) may be observed. Notably, the principal axis components, $\widetilde{R}^*_{xx}$ and $\widetilde{R}^*_{zz}$, have trends similar to the vertical component of turbulent mass flux velocity and species mass fraction flux. These components are positive over most of the domain, with the most intense regions located at the edges of the domain. The shear component, $\widetilde{R}^*_{xz}$, has a distribution similar to the horizontal component of turbulent mass flux velocity and species mass fraction flux, with a countergradient flux observed in the middle of the primary mixing layer. The most intense regions of $\widetilde{R}^*_{xz}$ are located within the plumes at the edges of the domain, similar to what was observed for $\widetilde{R}^*_{xx}$ and $\widetilde{R}^*_{zz}$.

2. Budget equation

The Favre-averaged Reynolds stress tensor transport equation is given by Besnard *et al.* [33] and here is reproduced from Wong *et al.* [34],

$$\underbrace{\frac{\partial \bar{\rho}\widetilde{R}_{ij}}{\partial t}}_{\text{term 1}} + \underbrace{\frac{\partial(\bar{\rho}\widetilde{u}_k\widetilde{R}_{ij})}{\partial x_k}}_{\text{term 2}} = \underbrace{a_i\left(\frac{\partial \bar{p}}{\partial x_j} - \frac{\partial \bar{\tau}_{jk}}{\partial x_k}\right) + a_j\left(\frac{\partial \bar{p}}{\partial x_i} - \frac{\partial \bar{\tau}_{ik}}{\partial x_k}\right)}_{\text{term 3a}} \underbrace{- \bar{\rho}\widetilde{R}_{ik}\frac{\partial \widetilde{u}_j}{\partial x_k} - \bar{\rho}\widetilde{R}_{jk}\frac{\partial \widetilde{u}_i}{\partial x_k}}_{\text{term 3b}}$$
$$\underbrace{- \frac{\partial(\overline{u_i' p'})}{\partial x_j} - \frac{\partial(\overline{u_j' p'})}{\partial x_i}}_{\text{term 4a}} \underbrace{+ \overline{p'\frac{\partial u_i'}{\partial x_j}} + \overline{p'\frac{\partial u_j'}{\partial x_i}}}_{\text{term 4b}} \underbrace{- \frac{\partial(\overline{\rho u_i'' u_j'' u_k''})}{\partial x_k}}_{\text{term 5a}}$$
$$\underbrace{+ \frac{\partial(\overline{u_i'\tau_{jk}'})}{\partial x_k} + \frac{\partial(\overline{u_j'\tau_{jk}'})}{\partial x_k}}_{\text{term 5b}} \underbrace{- \overline{\tau_{jk}'\frac{\partial u_i'}{\partial x_k}} - \overline{\tau_{ik}'\frac{\partial u_j'}{\partial x_k}}}_{\text{term 6}}. \tag{48}$$

These terms have once again been grouped to be approximately comparable to the similarly labeled terms used previously in this work. Term 1 represents the time rate of change, term 2 represents transport, term 3 represents production, term 4 represents redistribution, term 5 represents turbulent transport, and term 6 represents destruction. Note that, as with elsewhere in this paper, the terms containing neglected quantities are themselves neglected. This results in term 5b and term 6 being neglected here, in addition to the components of term 3a, which contain τ_{ij}. Terms 3 and 4 have also been split in a similar way to previous equations presented in this work. Terms 3a and 3b represent production by buoyancy and Reynolds stress. Terms 4a and 4b represent redistribution due to the pressure-strain correlation [38].

The tilt-compensated average profiles of each term in Eq. (48) are presented in Fig. 23 for each of the three resolved components of the stress tensor at $t^* = 1.241$ and $t^* = 1.744$. The horizontal normal stress component ($\widetilde{R}^*_{xx}$) is dominated by contributions from term 4, representing the combined redistribution term, with the production and turbulent transport terms representing a smaller contribution. This is similar to the trends observed in the horizontal component of the budget equations of turbulent mass flux velocity and species mass fraction flux. The vertical normal stress component ($\widetilde{R}^*_{zz}$) is dominated by production (term 3), though a non-negligible diffusive-like contribution from term 5 is also observed. This is again similar to the trends observed in the vertical components of the turbulent mass flux velocity and species mass fraction flux budget equations. The horizontal shear component ($\widetilde{R}^*_{xz}$) has approximately equal contributions from terms 3 and 4, with term 5 being the least significant contribution. Interestingly, the spatial distribution of $\widetilde{R}^*_{xz}$ demonstrates a countergradient momentum flux similar to what was observed for the transverse components of turbulent mass flux velocity and species mass fraction flux examined in this work. However, the dominant terms of the budget equations associated with these other quantities differ from the dominant terms in the budget for $\widetilde{R}^*_{xz}$. It is also interesting to note that the horizontal component is primarily dominated by redistribution (term 3), the shear stress component sees approximately equal contributions from production and redistribution, and the vertical normal stress component is dominated by the production term. A redistribution dominated transverse flow and a production-dominated vertical flow has been observed in other budget equations studied in the present work. The presence of a shear component is unique to the Reynolds stress tensor, however, and it is interesting to note that redistribution and production are of approximately equal importance for this component.

The production (term 3) and redistribution (term 4) terms may again be split into their "a" and "b" components to further examine the relative importance of these two terms for each component of the Reynolds stress tensor. These are presented in Fig. 24. It can be observed that production is dominated by production due to Reynolds stress for all resolved components, with the exception

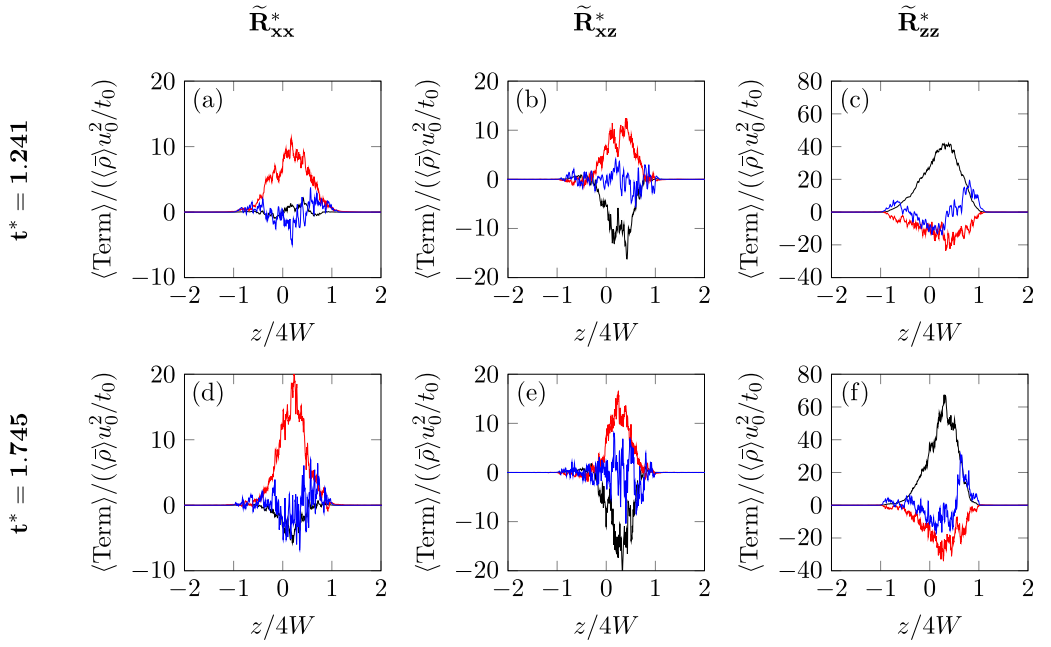

FIG. 23. Terms of the budget equation for the components of the Reynolds stress tensor [Eq. (48)] corresponding to the (left) horizontal normal stress ($\widetilde{R}^*_{xx}$), (center) $x-z$ shear stress ($\widetilde{R}^*_{xz}$), and (right) vertical normal stress ($\widetilde{R}^*_{zz}$) components at times (top): $t^* = 1.241$ and (bottom): $t^* = 1.745$. The black, red, and blue lines correspond to terms 3, 4, and 5 in the budget equation, respectively.

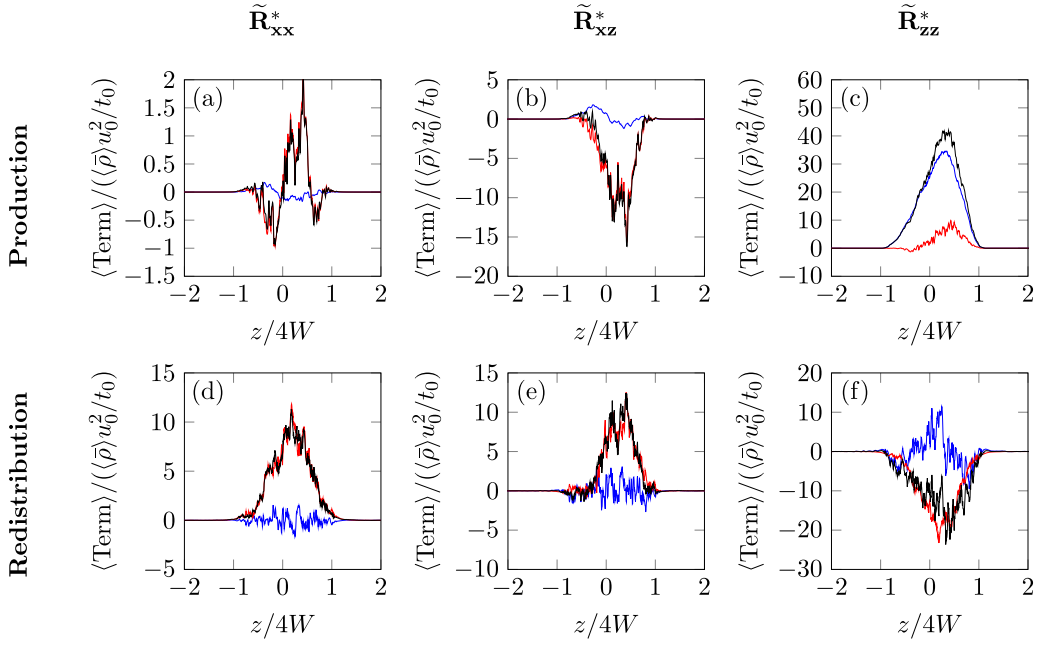

FIG. 24. Decomposition of (top) term 3 and (bottom) term 4 for the (left) horizontal normal stress ($\widetilde{R}^*_{xx}$), (center) x-z shear stress ($\widetilde{R}^*_{xz}$), and (right) vertical normal stress ($\widetilde{R}^*_{zz}$) components of the Favre-averaged Reynolds stress tensor. All plots are from $t^* = 1.241$. The blue and red lines indicate the "A" and "B" terms, respectively, and the black line indicates the sum of "A" and "B."

of the vertical principal stress component, $\widetilde{R}^*_{zz}$, where production due to buoyancy is dominant. Redistribution (term 4) is dominated by the contribution from the pressure-strain correlation term (term 4b) in almost all cases. The turbulent pressure strain correlation term (term 4a) is generally a much smaller contribution than term 4b, with the exception of the vertical normal stress component term where it plays a non-negligible role.

3. Reynolds anisotropy tensor

A final metric of interest concerns the isotropy of this flow. One way this can be examined is through the use of the normalized Reynolds anisotropy tensor. This is defined as [34,39]

$$b_{ij} = \frac{\widetilde{R}_{ij}}{2\widetilde{k}} - \frac{1}{3}\delta_{ij} = \frac{\widetilde{R}_{ij}}{\widetilde{R}_{kk}} - \frac{1}{3}\delta_{ij}, \tag{49}$$

where $\widetilde{R}_{ij}$ is the Favre-averaged Reynolds stress tensor, and δ_{ij} is the Kronecker delta. The components of the normalized Reynolds anisotropy tensor give a measure of the degree of anisotropy, or preferred directionality, of the flow. The principal axis components of the anisotropy tensor here do not appear to have significant spatial variation over the mixing layer. The distributions of the normalized Reynolds anisotropy tensor components for the two available diagonal components of the Reynolds stress tensor (b_{xx} and b_{zz}), as well as the shear stress component (b_{xz}), at two time instants corresponding to $t^* = 1.241$ and $t^* = 1.745$ is shown in Fig. 25. These figures are masked to show only regions where $0.01 \leqslant \widetilde{Y}_H \leqslant 0.99$, with b_{ij} set to 0 outside of these regions. This was done to restrict analysis to the region where mixing is occurring. A relatively constant value of b_{ij} is observed throughout the mixing layer for both the horizontal and vertical components. At later times, a slight difference in b_{ij} may be observed at the edges of the mixing layer versus the central region. It can also be observed that the vertical axis contains a substantially greater fraction of the total energy than the horizontal axis. Figure 26 depicts the tilt-compensated average profile of b_{ij} for $t^* = 1.241$ and $t^* = 1.745$ in order to more closely examine the distribution and values of b_{ij} across the central mixing layer. As with the pseudocolor plots, the lineout is masked to include only regions where $0.01 \leqslant \langle \widetilde{Y}_H \rangle \leqslant 0.99$. b_{ww}, representing the vertical axis, has an average value across the mixing layer of $b_{zz} \approx 0.28$, which a relatively constant value observed across the mixing layer width at $t^* = 1.241$. A similar value is observed at $t^* = 1.745$, though a greater variation in b_{zz} is observed across the mixing layer. b_{xx}, representing the horizontal axis, has a similarly constantly value across the mixing layer, though with a lower value of $b_{xx} \approx -0.14$, with this value being approximately the same for both time instances.

VI. CONCLUSIONS

Results from high-resolution simulations on the Tilted Rocket Rig experiment conducted using Miranda, a tenth-order compact finite difference hydrodynamics code, have been presented. These simulations seek to closely follow case 110 from the experiments of Smeeton and Youngs [1]. These simulations were conducted at several mesh resolutions in order to demonstrate convergence of the solution. Five parameters were used to establish temporal convergence of the solution. The first is the height of the rising spike of heavy fluid at the left edge of the domain and the falling bubble of light fluid at the right of the domain.

Good agreement between these simulations and experimental data is observed. Other metrics to demonstrate temporal convergence of the solution include integral mix width, the global mixing parameter, the amount of turbulent kinetic energy present in the flow, and the interface tilt angle. All of these metrics demonstrated good convergence with increasing grid resolution, as well as good agreement with previous simulations of this configuration [7]. Additional metrics to demonstrate spatial convergence of the solution include the spatial distributions of heavy fluid mass fraction and turbulent kinetic energy (TKE) at two fixed time instances. Both of these metrics also demonstrated good convergence at the highest resolution runs.

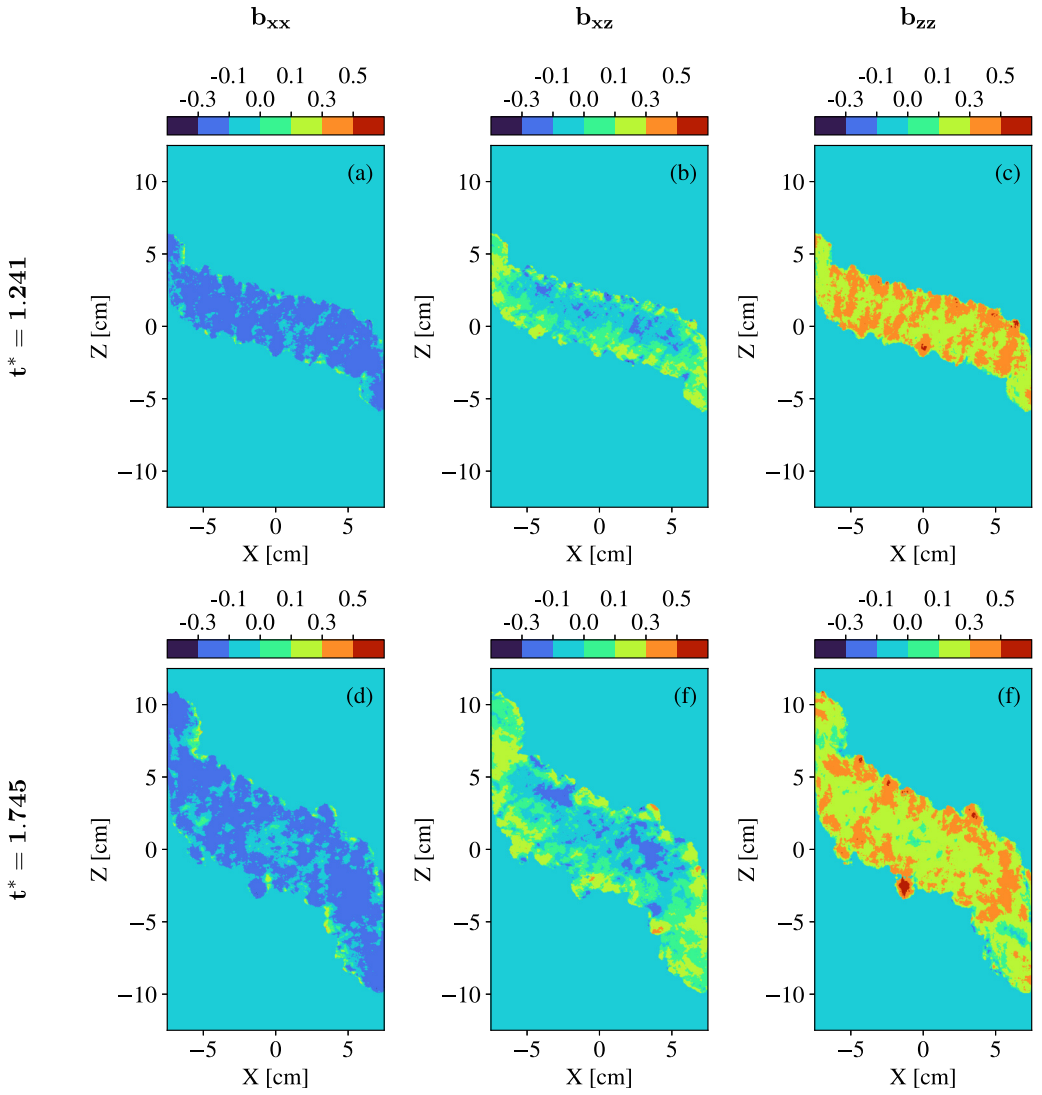

FIG. 25. Spatial distributions of the Reynolds anisotropy tensor [Eq. (49)] corresponding to (left) b_{xx}, (center) b_{xz}, and (right) b_{zz} at (top) $t^* = 1.241$ and (bottom) $t^* = 1.745$.

Analysis of these simulations has focused on both the spatial distribution of a number of flow variables relevant to the transport of mass and momentum in the mixing layer, including the turbulent mass flux velocity, turbulent species mass fraction flux, scalar variance, and Favre-averaged Reynolds stress tensor components, as well as the averaged behavior of the individual terms which comprise the unclosed budget equations for these quantities in the central mixing layer. The spatial distribution of the Favre-averaged Reynolds anisotropy tensor was also examined. This analysis was conducted at two times, corresponding to mid-time and late time in the development of the turbulent mixing layer.

The unclosed budget equations for the Favre-averaged Reynolds stress tensor terms were examined. The horizontal normal stress component is dominated by redistribution, the u-w shear stress component sees approximately equal contributions from production and redistribution, and the vertical normal stress component is dominated by the production terms. The redistribution term

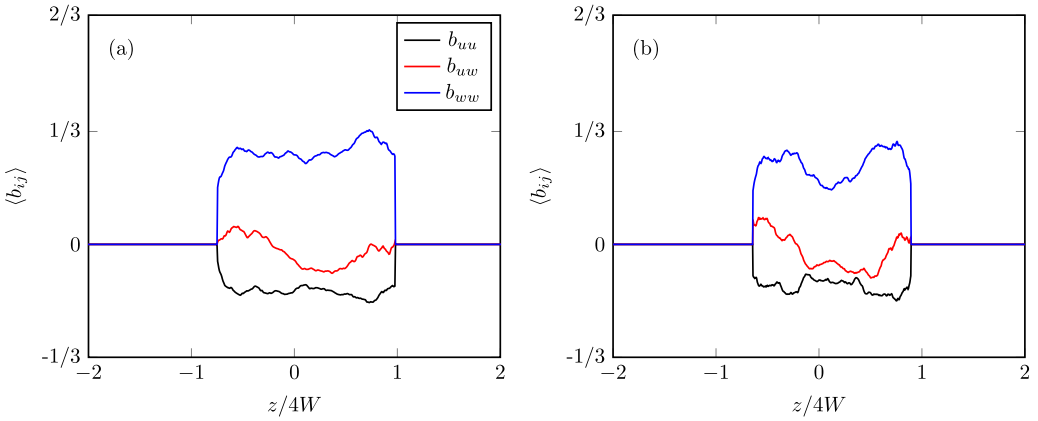

FIG. 26. Tilt-compensated averaged profiles of b_{ij} [Eq. (49)] for (a) $t^* = 1.241$ and (b) $t^* = 1.745$. This profile is equal to b_{ij} where $0.01 \leqslant \widetilde{Y}_H \leqslant 0.99$ and set to zero outside of this region.

in each of these cases is primarily dominated by the pressure-strain correlation term, although the vertical normal stress component does see a non-negligible contribution from a turbulent pressure strain correlation term as well.

Additionally, examination of the directionality of the flow using the Favre-averaged Reynolds anisotropy tensor was conducted. The distribution of anisotropy is found to be relatively constant across the mixing layer. The vertical component of the flow is found to have a majority of the energy, with a value of $b_{zz} \approx 0.28$ across the central mixing layer. The horizontal component has a value of $b_{xx} \approx -0.14$, with this value being relatively constant across the mixing layer.

The spatial distributions of turbulent mass flux velocity, as well as the turbulent species mass fraction flux, are observed to be similar. The horizontal components demonstrate a countergradient flux in the upper half of the central mixing layer for both metrics. This behavior for the turbulent mass flux velocity has been previously reported by Denissen *et al.* [8]. The vertical components of both of these quantities are similar, with a general trend showing an upwards flux of each. The spatial distribution of the Favre-averaged Reynolds stress tensor shows similar trends to these quantities as well, with the principal stress components being similar to the vertical components of turbulent mass flux velocity and species mass fraction flux, and the shear stress component being similar to the horizontal component of these fields.

The unclosed budget equations for turbulent mass flux velocity and turbulent species mass fraction flux are also analyzed. The vertical components of these budget equations are dominated by production, while the transverse components are dominated by redistribution. The production and redistribution terms have also been analyzed term by term in order to examine the relative influence of each term. In the vertical axis, where production is dominant, it is found that production due to buoyancy and Reynolds stresses comprise approximately equal parts of the total production term. A different trend is observed in the transverse axis, where the redistribution term is primarily influenced by a single term. This term is frequently neglected as part of Reynolds-averaged Navier-Stokes modeling. This result indicates that inclusion of this term in the models is important in order to accurately predict two dimensional mixing.

ACKNOWLEDGMENTS

This work was performed under the auspices of the U.S. Department of Energy by Lawrence Livermore National Laboratory under Contract DE-AC52-07NA27344. The authors would like to acknowledge the useful conversations with Dr. Britton Olson.

APPENDIX: SENSITIVITY OF SIDEWALL BUBBLE AND SPIKE HEIGHTS TO THRESHOLD CHOICE

A potential source of the disagreement between the simulation results and the experimental data may arise from differences in how h_b and h_s are calculated, particularly the thresholds chosen to identify the edge of the spike and bubble plumes. It is therefore useful to examine the sensitivity of results to changing the threshold used. Two approaches are used to examine this influence. First, the bubble and spike amplitudes are found by utilizing the prescription of Andrews *et al.* [7] with thresholds of 99.9/0.01% and 99/1%. One aspect of note is that this method results in the bubble and spike plumes manifesting as small "tails" in the averaged mass fraction data as they occupy only a small part of the domain width. Consequently, this method does not work as well for thresholds less sensitive than 99/1%, which may not be representative of the experimental analysis. A representative plot of $\langle Y_H \rangle$ is shown in Fig. 27, which depicts these tails and illustrates how less sensitive thresholds will not correctly detect the location of the sidewall bubble and spikes. A second method which is more resilient to less sensitive thresholds involves selecting the first 10% (spike) or last 10% (bubble) of the data along the x axis. This has the effect of reducing the data to only the region containing the spike or bubble plumes. This subselected data is then averaged using Eq. (34) to produce a profile of average heavy mass fraction as a function of the vertical (z) coordinate in this subselected region. This approach results in the spike or bubble plumes comprising a greater percentage of the data that is averaged, and therefore increases their influence in the averaged profiles. This, in turn, allows for less sensitive thresholds to be utilized which may be more comparable to those used in the experiment. The thresholds used are the crossings of 99.1/0.01%, 99/1%, 95/5%, and 90/10% averaged heavy mass fraction. A comparison between bubble and spike heights for the two methods and different thresholds from the R16 mesh, together with the experimental data, is presented in Fig. 28.

Generally, increasing the threshold values appears to result in slight decreases to the bubble and spike heights, as expected, although large differences in bubble and spike heights are not observed across different threshold values. The results of the 99.9/0.01% threshold using the entire domain and the 99/1% using the subselected domain appear to agree well. This is similarly true for the 99% whole domain and 95% subselected domain results. The 99% (whole domain)/95% (subselected)

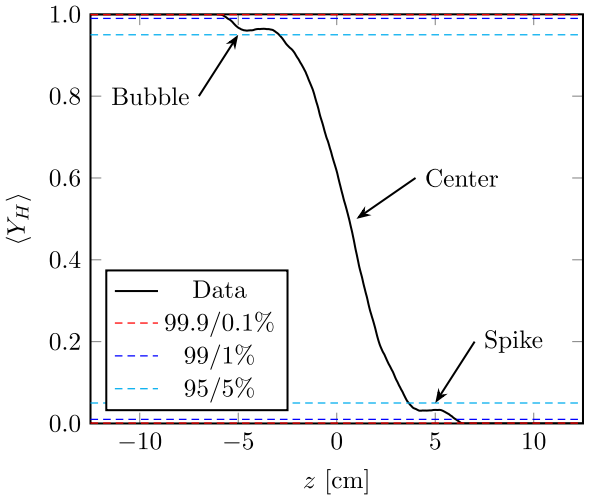

FIG. 27. Profile of $\langle Y_H \rangle$ with the average taken over the whole domain. The "tails" representing the sidewall spike and bubble are visible. Note that these features fall below the 5% threshold and so would not be correctly detected.

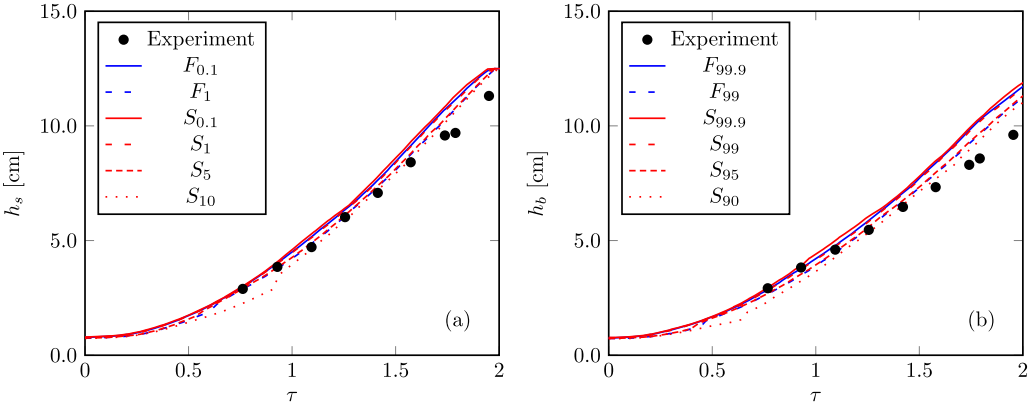

FIG. 28. Heights of the (a) rising spike of heavy fluid on the left side of the domain and (b) falling bubble of light fluid on the right side of the domain as a function of analysis method and threshold. F corresponds to profiles using the full domain, S corresponds to profiles obtained by subselecting the data, and the subscript denotes the threshold value of $\langle Y_H \rangle$ used to determine the location of the bubble or spike. Experimental data from Smeeton and Youngs [1] (reproduced from Andrews *et al.* [7]) are presented for comparison.

results also appear to have a better agreement with experimental data at early through middle times, though late-time disagreement is still observed. In general, the observed improved agreement for early to mid-times is likely due to this threshold being closer to the threshold used in the experiment.

[1] V. S. Smeeton and D. L. Youngs, Experimental investigation of turbulent mixing by Rayleigh-Taylor instability III, AWE Report No. O 35/87, Atomic Weapons Establishment, 1987.

[2] D. L. Youngs, Modelling turbulent mixing by Rayleigh-Taylor instability, Physica D **37**, 270 (1989).

[3] Lord Rayleigh, Investigation of the character of the equilibrium of an incompressible heavy fluid of variable density, Proc. London Math. Soc. **s1-14**, 170 (1883).

[4] G. I. Taylor, The instability of liquid surfaces when accelerated in a direction perpendicular to their planes. I, Proc. R. Soc. Lond. A **201**, 192 (1950).

[5] Y. Zhou, Rayleigh-Taylor and Richtmyer-Meshkov instability induced flow, turbulence, and mixing. I, Phys. Rep. **720–722**, 1 (2017).

[6] Y. Zhou, Rayleigh-Taylor and Richtmyer-Meshkov instability induced flow, turbulence, and mixing. II, Phys. Rep. **723–725**, 1 (2017).

[7] M. J. Andrews, D. L. Youngs, D. Livescu, and T. Wei, Computational studies of two-dimensional Rayleigh-Taylor driven mixing for a tilted-rig, J. Fluids Eng. **136**, 091212 (2014).

[8] N. A. Denissen, B. Rollin, J. M. Reisner, and M. J. Andrews, The Tilted Rocket Rig: A Rayleigh-Taylor test case for RANS models, J. Fluids Eng. **136**, 091301 (2014).

[9] I. W. Kokkinakis, D. Drikakis, and D. L. Youngs, Modeling of Rayleigh-Taylor mixing using single-fluid models, Phys. Rev. E **99**, 013104 (2019).

[10] M. Xiao, Y. Zhang, and B. Tian, Modeling of turbulent mixing with an improved K-L model, Phys. Fluids **32**, 092104 (2020).

[11] H.-s. Xie, M.-j. Xiao, and Y.-s. Zhang, Unified prediction of turbulent mixing induced by interfacial instabilities via Besnard-Harlow-Rauenzahn-2 model, Phys. Fluids **33**, 105123 (2021).

[12] M. Xiao, Y. Zhang, and B. Tian, A K-L model with improved realizability for turbulent mixing, Phys. Fluids **33**, 022104 (2021).

[13] A. W. Cook, Artificial fluid properties for large-eddy simulation of compressible turbulent mixing, Phys. Fluids **19**, 055103 (2007).

[14] A. W. Cook, Enthalpy diffusion in multicomponent flows, Phys. Fluids **21**, 055109 (2009).

[15] W. H. Cabot and A. W. Cook, Reynolds number effects on Rayleigh-Taylor instability with possible implications for type-Ia supernovae, Nat. Phys. **2**, 562 (2006).
[16] B. E. Morgan, B. J. Olson, J. E. White, and J. A. McFarland, Self-similarity of a Rayleigh-Taylor mixing layer at low Atwood number with a multimode initial perturbation, J. Turbul. **18**, 973 (2017).
[17] B. E. Morgan, B. J. Olson, W. J. Black, and J. A. McFarland, Large-eddy simulation and Reynolds-averaged Navier-Stokes modeling of a reacting Rayleigh-Taylor mixing layer in a spherical geometry, Phys. Rev. E **98**, 033111 (2018).
[18] B. E. Morgan, Simulation and Reynolds-averaged Navier-Stokes modeling of a three-component Rayleigh-Taylor mixing problem with thermonuclear burn, Phys. Rev. E **105**, 045104 (2022).
[19] A. W. Cook, W. H. Cabot, and P. L. Miller, The mixing transition in Rayleigh-Taylor instability, J. Fluid Mech. **511**, 333 (2004).
[20] B. J. Olson and A. W. Cook, Rayleigh–Taylor shock waves, Phys. Fluids **19**, 128108 (2007).
[21] B. J. Olson, J. Larsson, S. K. Lele, and A. W. Cook, Nonlinear effects in the combined Rayleigh-Taylor/Kelvin-Helmholtz instability, Phys. Fluids **23**, 114107 (2011).
[22] V. K. Tritschler, B. J. Olson, S. K. Lele, S. Hickel, X. Y. Hu, and N. A. Adams, On the Richtmyer-Meshkov instability evolving from a deterministic multimode planar interface, J. Fluid Mech. **755**, 429 (2014).
[23] B. J. Olson and J. Greenough, Large eddy simulation requirements for the Richtmyer-Meshkov instability, Phys. Fluids **26**, 044103 (2014).
[24] B. J. Olson and J. A. Greenough, Comparison of two- and three-dimensional simulations of miscible Richtmyer-Meshkov instability with multimode initial conditions, Phys. Fluids **26**, 101702 (2014).
[25] A. Campos and B. E. Morgan, Direct numerical simulation and Reynolds-averaged Navier-Stokes modeling of the sudden viscous dissipation for multicomponent turbulence, Phys. Rev. E **99**, 063103 (2019).
[26] B. E. Morgan, Large-eddy simulation and Reynolds-averaged Navier-Stokes modeling of three Rayleigh-Taylor mixing configurations with gravity reversal, Phys. Rev. E **106**, 025101 (2022).
[27] D. Livescu, T. Wei, and M. R. Petersen, Direct Numerical Simulations of Rayleigh-Taylor instability, J. Phys.: Conf. Ser. **318**, 082007 (2011).
[28] G. Dimonte, D. L. Youngs, A. Dimits, S. Weber, M. Marinak, S. Wunsch, C. Garasi, A. Robinson, M. J. Andrews, P. Ramaprabhu *et al.*, A comparative study of the turbulent Rayleigh-Taylor instability using high-resolution three-dimensional numerical simulations: The Alpha-Group collaboration, Phys. Fluids **16**, 1668 (2004).
[29] P. Ramaprabhu, G. Dimonte, and M. J. Andrews, A numerical study of the influence of initial perturbations on the turbulent Rayleigh-Taylor instability, J. Fluid Mech. **536**, 285 (2005).
[30] D. Layzer, On the instability of superposed fluids in a gravitational field, Astrophys. J. **122**, 1 (1955).
[31] V. N. Goncharov, Analytical Model of Nonlinear, Single-Mode, Classical Rayleigh-Taylor Instability at Arbitrary Atwood Numbers, Phys. Rev. Lett. **88**, 134502 (2002).
[32] M. J. Andrews and D. B. Spalding, A simple experiment to investigate two-dimensional mixing by Rayleigh–Taylor instability, Phys. Fluids **2**, 922 (1990).
[33] D. Besnard, F. H. Harlow, R. M. Rauenzahn, and C. Zemach, *Turbulence transport equations for variable-density turbulence and their relationship to two-field models*, Los Alamos Tech. Rep. No. LA-12303-MS, Los Alamos National Lab. (LANL), Los Alamos, USA, 1992.
[34] M. L. Wong, J. R. Baltzer, D. Livescu, and S. K. Lele, Analysis of second moments and their budgets for Richtmyer-Meshkov instability and variable-density turbulence induced by reshock, Phys. Rev. Fluids **7**, 044602 (2022).
[35] B. E. Morgan and M. E. Wickett, Three-equation model for the self-similar growth of Rayleigh-Taylor and Richtmyer-Meskov instabilities, Phys. Rev. E **91**, 043002 (2015).
[36] N. O. Braun and R. A. Gore, A multispecies turbulence model for the mixing and de-mixing of miscible fluids, J. Turbul. **22**, 784 (2021).
[37] T. Poinsot and D. Veynante, *Theoretical and Numerical Combustion*, 2nd ed. (Edwards, Philadelphia, PA, 2005).
[38] C. G. Speziale, S. Sarkar, and T. B. Gatski, Modelling the pressure-strain correlation of turbulence: An invariant dynamical systems approach, J. Fluid Mech. **227**, 245 (1991).
[39] S. B. Pope, *Turbulent Flows* (Cambridge University Press, Cambridge, 2000).